Gravitational Wave Probes of a Classically Conformal Standard Model Extension

Bachelorarbeit
zur Erlangung des akademischen Grades
Bachelor of Science (B.Sc.) in Physik
am Institut für Theoretische Physik (ITP)
der Goethe-Universität Frankfurt am Main

vorgelegt von

Tamara Caldas Cifuentes

aus Mörfelden-Walldorf

eingereicht am 3. Juni 2022
Erstgutachterin: Prof. Dr. Laura Sagunski
Zweitgutachter: Prof. Dr. Jürgen Schaffner-Bielich

Abstract

In this work, we study the stochastic gravitational wave background induced by a first-order phase transition in the framework of the Classically Conformal $U(1)_{\mathrm{B-L}}$-extention of the Standard Model of particle physics. Moreover, we predict their detectability w.r.t the future gravitational-waves observatory LISA by computing the corresponding signal-to-noise ratios.

Zusammenfassung

In dieser Arbeit untersuchen wir die Gravitationswellensignale kosmologischer Phasenübergänge erster Ordnung im Rahmen der klassisch konformalen $U(1)_{\mathrm{B-L}}$-Standardmodellerweiterung. Des Weiteren überprüfen wir ihre Detektierbarkeit mit dem zukünftigen Gravitationswellenobservatorium LISA, indem wir ihre Signal-Rausch-Verhältnisse berechnen.

Selbstständigkeitserklärung

Hiermit erkläre ich, dass ich die Arbeit selbstständig und ohne Benutzung anderer als der angegebenen Quellen und Hilfsmittel verfasst habe. Alle Stellen der Arbeit, die wörtlich oder sinngemäß aus Veröffentlichungen oder aus anderen fremden Texten entnommen wurden, sind von mir als solche kenntlich gemacht worden. Ferner erkläre ich, dass die Arbeit nicht - auch nicht auszugsweise - für eine andere Prüfung verwendet wurde.

Mörfelden-Walldorf, den 3. Juni 2022

_____

Tamara Caldas Cifuentes

Acronyms

B-L Baryon number minus lepton number

dofs Degrees of freedom

EOM Equation of motion

EOS Equation of state

EWPT Electroweak phase transition

FMEq Friedmann equations

LG Lorentz gauge

PT Phase transition

QFT Quantum field theory

SM Standard Model of particle physics

SSB Spontaneous symmetry breaking

TQFT Thermal quantum field theory

TTG TT- (*transverse-traceless*) gauge

VEV Vacuum expectation value

w.r.t. with respect to

Contents

1 Motivation

Our current understanding of the natural world is based on Einstein's theory of General Relativity and the Standard Model of particle physics (SM). The latter describes the elementary particles which make up the matter around us. However, there are still plenty of open questions that cannot be answered within this framework, e.g. like *Baryogenesis*, the *Hierachy problem*, the nature of *dark matter* etc.. This suggests that the SM must be incomplete. Today, large particle accelerators are used to observe and discover high energy physics phenomena. In general, the reachable experimental energy scales are limited. However, we know that there must have existed another high energy particle laboratory we might be able to access in a whole new way: the early Universe.

Some processes in the early Universe generate *gravitational waves* (GW). Their signals contain information about the process itself as well as the underlying fundamental theory. As a consequence, if we are able to predict and observe these GW signals, we will be able to extract all this information and probe our theories.

The Classically Conformal $B − L$**-SM Extension.** In this work, we investigate the Classically Conformal $B − L$-SM extension which has been subject to research for several years (see for example [1–3]). We will explain its key feautures in Section 3. It is well-motivated, provides an elegant solution to the Hierachy problem and might offer answers to the open Baryogenesis question. Most importantly, the GW signals of the possible first-order phase transitions (PT) in this model might be probeable by the future space-based GW observatory *Laser Interferometer Space Antenna* (LISA). Its frequency domain lies in the millihertz regime, i.e. $f \in [10^{-5} \, \text{Hz}, 1 \, \text{Hz}]$, and might be suited to detect the stochastic gravitational wave background of cosmological origins.

2 Theoretical framework

2.1 Gravitational waves

Mass tells spacetime how to curve. Spacetime tells matter how to move.
- J. A. Wheeler

In General Relativity, gravity is understood as the interplay between energy and the curvature of spacetime. This relation is beautifully formulated in the Einstein equations: $G_{\mu\nu} = 8\pi G T_{\mu\nu}$[1]. The Einstein tensor $G_{\mu\nu}$ that contains information about the spacetime's metric (and thus its curvature) is directly linked to the energy-momentum tensor $T_{\mu\nu}$, which encodes the energy content of the Universe. We can expand the metric tensor (weak-field ansatz) via

$$g_{\mu\nu} = \eta_{\mu\nu} + h_{\mu\nu}, \quad |h_{\mu\nu}| \ll 1, \quad h_{\mu\nu} = h_{\nu\mu}, \tag{1}$$

where $\eta_{\mu\nu} = \mathrm{diag}(-1, 1, 1, 1)$ is the Minkowski metric and $h_{\mu\nu}$ is a small tensor pertubation in flat spacetime. Inserting this expression into the Einstein equations and keeping terms only up to linear order yields a fascinating theoretical result: The complex field equations reduce to a wave equation[2] for the metric pertubation tensor $h_{\mu\nu}$ whose solutions we call *gravitational waves* (GW) [4],

$$(T_{\mu\nu} = 0) \quad \Box \bar{h}_{\mu\nu} = 0. \tag{2a}$$

$$(T_{\mu\nu} \neq 0) \quad \Box \bar{h}_{\mu\nu} = -16\pi G \, T_{\mu\nu}, \tag{2b}$$

In the derivation of Eq. (2a) and (2b), we have made use of the theory's *gauge freedom*, i.e. the freedom of choice of coordinates and certain transformations, by introducing the *trace-reverse* metric pertubation $\bar{h}_{\mu\nu}$ and the *Lorenz* gauge (LG)[3],

$$\bar{h}_{\mu\nu} \equiv h_{\mu\nu} - \frac{1}{2}\eta_{\mu\nu}, \tag{3a}$$

$$\partial^\nu \bar{h}_{\mu\nu} = \partial_\nu \bar{h}^{\mu\nu} = \bar{h}_{\mu\nu,\nu} = 0, \tag{3b}$$

respectively. The general solutions of (2a) and (2b), are [5]

$$(T_{\mu\nu} = 0) \quad \bar{h}_{\mu\nu}(t, \mathbf{x}) = \mathrm{Re}\left[\mathcal{A}e_{\mu\nu}\exp\left(ik_\gamma x^\gamma\right)\right], \tag{4a}$$

$$(T_{\mu\nu} \neq 0) \quad \bar{h}_{\mu\nu}(t, \mathbf{x}) = 4G \int d^3\mathbf{y} \, \frac{T_{\mu\nu}(t_r, \mathbf{y})}{|\mathbf{x} - \mathbf{y}|}. \tag{4b}$$

---

[1]Note that in this work, we make use of natural units where $\hbar = 1 = c$.

[2]The *D'Alembert operator* in flat spacetime (and cartesian coordinates) is defined as $\Box \equiv \eta^{\mu\nu}\partial_\mu\partial_\nu = \left(-\partial_t^2 + \nabla^2\right)$.

[3]Other common names are *Hilbert* gauge or *De Donder* gauge. We can also formulate it without the use of Eq. (3a), namely $0 = \partial_\nu h^{\mu\nu} - \frac{1}{2}\partial^\mu h$, where $h \equiv \eta^{\mu\nu}h_{\mu\nu}$ is the metric pertubation tensor's trace.

The vacuum solution (4a) is (the real part of) a plane wave that is characterized by an amplitude $\mathcal{A}$, its *polarization tensor* $e_{\mu\nu}$ and the *wave vector* k^γ. The source-case solution (4b) is the 'retarded Greens integral', where $\mathbf{x}$ is the measuring position, $\mathbf{y}$ is the position of the source, $T_{\mu\nu}$ is the energy-momentum tensor of the source and $t_r = t - |\mathbf{x} - \mathbf{y}|$ is the *retarded* time.

2.1.1 Influence of a gravitational wave on particles

It is insightful to study the effect of GWs on particles in the case of Eq. (2a) and hence Eq. (4a). This is applicable if the observer is far away from the source of the GW. The symmetry of the metric pertubation tensor, $h_{\mu\nu} = h_{\nu\mu}$, and Eq. (3b) impose constraints on our solution, namely its 'light-like'-ness and *orthogonality*, i.e.

$$k_\gamma k^\gamma \;=\; 0 \text{ and } \quad e^{\mu\nu} k_\nu \;=\; 0 \,. \tag{5}$$

However, it turns out that our gauge freedom is still not exhausted - we can add more restrictions to the polarization tensor $e_{\mu\nu}$ via the *TT*-gauge (TTG), in which it becomes *transverse* and *traceless*, i.e.

$$e^{0\mu} \;\equiv\; 0 \;\Rightarrow\; e^{0i} k_i \;=\; 0 \quad \text{and} \quad \eta_{\mu\nu}\, e^{\mu\nu} \;\equiv\; 0 \;\Rightarrow\; \bar{h}^{\mathrm{TT}}_{\mu\nu} \;=\; h^{\mathrm{TT}}_{\mu\nu} \,. \tag{6}$$

This operation reduces the number of independent components in $h_{\mu\nu}$ from originally 16 to $16 - 6 - 4 - 4 = 2$ (due to its symmetry, the LG and TTG). Finally, we end up with only two physical degrees of freedom called the *two polarizations* of a GW, commonly referred to as +-polarization and ×-polarization. Hence, a general solution will be a linear combination of both. We can study the impact of a GW on two test masses separated by a vector ξ^μ by looking at its geodesic deviation equation [4],

$$\frac{d^2 \xi^i}{dt^2} = R^i_{0j0}\, \xi^j = \frac{1}{2}\, \partial_t^2 h^{\mathrm{TT}i}_{\;\;\;j}\, \xi^j. \tag{7}$$

In the case of a purely +-polarized GW propagating in the z-direction with wave vector $k^\gamma = (\omega, 0, 0, \omega)$, the resulting polarization tensor is [5]

$$e_{\mu\nu} = \begin{pmatrix} 0 & 0 & 0 & 0 \\ 0 & H_+ & H_\times & 0 \\ 0 & H_\times & -H_+ & 0 \\ 0 & 0 & 0 & 0 \end{pmatrix}, \tag{8}$$

and the metric it produces reads [4]

$$ds^2 \;=\; -dt^2 + (1 + h_+)dx^2 + (1 + h_\times)dy^2 + dz^2, \tag{9}$$

where $h_+ \;=\; \mathcal{A}\, H_+ \exp\left(-i\omega(t - z)\right)$. It is now possible to solve Eq. (7) perturbatively for small H_+ and we find that [5]

$$\frac{d^2 \xi^1}{dt^2} = -\frac{\omega^2}{2} H_+ e^{i\omega t} \xi^1 \quad \Rightarrow \quad \xi^1(t) = \xi^1(0)\left(1 + \frac{1}{2} H_+ e^{i\omega t} + \ldots\right) \tag{10}$$

$$\frac{d^2 \xi^2}{dt^2} = +\frac{\omega^2}{2} H_+ e^{i\omega t} \xi^2 \quad \Rightarrow \quad \xi^2(t) = \xi^2(0)\left(1 - \frac{1}{2} H_+ e^{i\omega t} + \ldots\right) \tag{11}$$

Imagine the situation where a number of particles are distributed along a circle with radius $R^2 = \xi^1(0) + \xi^2(0)$ as shown in Fig. 1. From Eq. (10) and Eq. (11) we see that the presence of GW will periodically deform the initial circle to an ellipse.

▶ Finally, we conclude that GWs produce periodic curvature deformations in space-time that generate tidal forces acting on masses. Their proper separation distance will then oscillate with time (see also Fig. 2). This is also the basic concept of how GWs are measured in experiments.
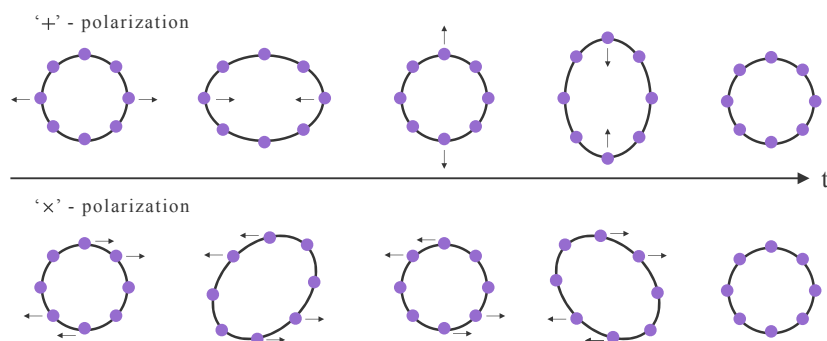
Figure 1: Schematic visualization of the impact of a gravitational wave on a ring with masses. It periodically deforms the initial circular arrangement of masses to an elliptical shape. This can happen in either a +- or ×-pattern.
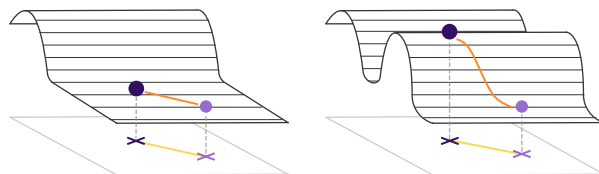

Figure 2: In the TT-gauge, when a GW passes by, the *coordinate* separation distance (yellow) between two particles does not change, whereas their *proper* separation distance (orange) changes with time. For more details, see [6, 7].

2.1.2 Gravitational wave detection

The basic concept of GW detection is the *periodic change of proper distance or proper time* in the presence of a GW. It is realized in several types of experiments: bar detectors, laser interferometer and pulsar timing arrays (PTAs). Here, we want to focus on the inteferometer experiments (see Fig. 3): An interferometer is an apparatus that has long orthorgonal 'arms' with cavities into which laser light is emitted, split up in separate beams and eventually reflected at the end. The light beams are then reunited and interfere with each other (Michelson interferometer). The variation of the *return time* of the light beams is then visible in the change of the resulting interference pattern, which is being detected by the photodetector. This is the case when GWs are passing by the experiment, since the periodic change in proper distance will be reflected in changing return times. According to [4], in the case of a purely +-polarized GW moving in the z-direction, the variation of the return time is given by

Figure 3: Scheme of the main ingredients for a simple Michelson-interferometer. [7]

$$\frac{dt_{\text{return}}}{dt} = 1 + \frac{1}{2}\left[h_+(t+2L) - h_+(t)\right], \tag{12}$$

where L is the fixed coordinate length of one arm.[4] The detector's capabilities are limited by multiple noise sources such as thermal noise (due to finite temperature), quantum noise, gravity gradient noise (due to earth-based fluctuations of the local gravitational field) and ground vibration and mechanical noise. The latter can be avoided in future space-based interferometers like the *Laser Interferometer Space Antenna* (LISA).

Experiment	ρ_{thr}	t_{obs} / yrs	f_{min} / Hz	f_{max} / Hz
LISA	10	4	10^{-5}	1
DECIGO	10	4	10^{-2}	10^2
B-DECIGO	8	4	10^{-3}	10^2

Table 1: Experimental data from different GW experiments [8].

---

[4]In the case of the space-based LISA experiment ($L = 4$ km), the measureable change in the arm's length δl_{GW} due to a GW would be of the order $\mathcal{O}(10^{-18}$ m). [4]

2.1.3 Gravitational waves in non-vacuum

If the observer of a GW is relatively close to its source, we have the case of Eq. (2b). Equations (2a) and (2b) imply that GW can either be a source of energy and momentum or likewise be generated by a source with an according energy-momentum tensor $T_{\mu\nu}$. Examples for the latter are *astrophysical sources* like the inspiral of a merging binary system or *cosmological sources*, e.g. bubble collisions in cosmological phase transitions (see Sec 2.3.4). Suppose our source is localized in a volume Σ and our measuring point $\mathbf{x}$ is far away from it such that $r \equiv |\mathbf{x}| \gg d$, where d is the size of the source. We can then approximate Eq. (4b) in terms of

$$|\mathbf{x} - \mathbf{y}| = r - \frac{\mathbf{x} \cdot \mathbf{y}}{r} \ldots \quad \Rightarrow \quad \frac{1}{|\mathbf{x} - \mathbf{y}|} = \frac{1}{r} + \frac{|\mathbf{x} - \mathbf{y}|}{r^3} \ldots \tag{13}$$

The dynamics are fully encoded in the spatial part of $\bar{h}_{\mu\nu}$ [5],

$$\bar{h}_{\mu 0} = \text{const.}^5, \quad \bar{h}_{ij}(t, \mathbf{x}) \approx \frac{4G}{r} \int_{\Sigma} d^3y \; T_{ij}(t - r, \mathbf{y}) = \frac{2G}{r} \frac{d^2 I_{ij}}{dt^2}(t_r), \tag{14}$$

where

$$I_{ij}(t_r) = \int_{\Sigma} d^3y \; T_{00}(t_r, \mathbf{y}) \; y_i y_j = \int_{\Sigma} d^3y \; \rho(t_r, \mathbf{y}) \; y_i y_j \tag{15}$$

is the *mass quadrupole moment* (at retarded time). Hence, gravitational radiation is created by the time-dependent quadrupole moment of the source. This is why Eq. (14) is referred to as the *quadrupole formula* and Eq. (13) as the *quadrupole approximation*. An important consequence is that spherically symmetric sources are not able to produce GWs, even if they are dynamical (see *Birkhoff theorem* [9]). For GWs, we need asymmetric processes!

---

[5]This follows from the conservation of energy and momentum. For further details, see [6].

2.2 Cosmology

2.2.1 Geometry and dynamics

In order to parametrize the expansion of the Universe, we need to find a time-dependent solution of Einstein's equations. Assuming isotropy and homogenity on large scales (~ 100 Mpc)[6] yields a metric describing maximally symmetric spatial slices $\Sigma(t)$ evolving with the *scale factor* $a(t)$. It is called the Friedmann-Lemaître-Robertson-Walker (FLRW) metric and reads

$$ds^2 = dt^2 - a(t)^2 \left[\frac{dr^2}{1 - kr^2} + r^2 d\Omega^2 \right] = dt^2 - a(t)^2 d\zeta^2. \tag{16}$$

In accordance with isotropy and homogenity, we can additionally introduce the *perfect fluid energy-momentum tensor* $T_{\mu\nu} = \text{diag}(\rho, -p, -p, -p)$ (in the rest frame of the fluid) to solve the Einstein equations. The results are the dynamical equations for the scale factor a called the *Friedmann equations* (FMEqs)

$$H^2 = \left(\frac{\dot{a}}{a} \right)^2 = \frac{8\pi G}{3} \rho - \frac{k}{a^2} = \frac{\rho}{3M_{\text{pl}}^2} - \frac{k}{a^2}, \tag{17a}$$

$$\frac{\ddot{a}}{a} = -\frac{4\pi G}{3}(\rho + 3P), \tag{17b}$$

where G is Newton's constant, $M_{\text{pl}} \equiv \sqrt{1/8\pi G}$ is the Planck mass, $k \in \{0, \pm 1\}$ is the Universe's curvature parameter[7], and $\rho = \sum_i \rho_i$ and $P = \sum_i P_i = \sum_i w_i \rho_i$ are the total energy density and pressure as the sums of the individual contributions. Here we have also imposed an equation of state (EOS) with the EOS-parameter w_i whose value depends on the content it describes. The scale factor's evolution is determined by the energy content in the Universe. In the so-called ΛCDM-model, we divide it into three main categories: *matter* (m) that represents non-relativistic baryonic and cold collisionless dark matter (CDM) particles, *radiation* (r) denoting relativistic particles, and *dark energy* (Λ) which describes a yet unknown type of energy source exerting a negative pressure, like the cosmological constant Λ. Assuming one species dominates the others, $\rho \approx \rho_i$, we can solve the FMEqs and obtain a relation telling us how the energy density scales with a (see Table 2.2.1), namely $\rho_i \propto a^{-3(1+w_i)}$. We then find that there must have been three major epochs in the Universe's history dominated by either radiation, matter or dark energy (see Fig 4). Using the solutions for ρ_i from Table 2.2.1 as well as the definition of the critical energy density $\rho_{\text{crit}} \equiv 3H_0^2/8\pi G$ and dividing Eq. (17a) by H_0^2, we can rewrite Eq. (17a) as

$$\frac{H^2}{H_0^2} = \sum_i \Omega_{i,0} \left(\frac{a_0}{a} \right)^{3(1+w_i)} = \Omega_{r,0} \left(\frac{a_0}{a} \right)^4 + \Omega_{m,0} \left(\frac{a_0}{a} \right)^3 + \Omega_{\Lambda,0}, \tag{18}$$

---

[6]These conditions are also known as the *cosmological principle*.

[7]We distinguish three cases: i) $k = 0$ (*flat* Universe), ii) $k = +1$ (*closed* Universe) and iii) $k = -1$ (*open* Universe). Henceforth, we set $k = 0$ for convenience and since it suits current observations best. [10]

Quantity	Matter (m)	Radiation (r)	Dark Energy[9](Λ)
EOS-parameter w	≈ 0	1/3	-1
Density parameter Ω_0	0.32 [11]	9.4×10^{-5} [11]	0.68 [11]
Energy density ρ	$\rho_r(a) = \rho_{m,0}\, a^{-3}$	$\rho_r(a) = \rho_{r,0}\, a^{-4}$	$\rho_\Lambda(a) = \rho_{\Lambda,0}$
Scale factor $a(t)$	$a(t) \propto t^{2/3}$	$a(t) \propto t^{1/2}$	$a(t) \propto \exp(H_0 t)$

Table 2: Main ingredients of our Universe.

where we introduced the dimensionless denisty parameters Ω_i

$$\Omega_i = \frac{\rho_i}{\rho_{\text{crit}}}, \quad \Omega_{i,0} = \frac{\rho_{i,0}}{\rho_{\text{crit},0}} = \frac{\rho_i}{\rho_{\text{crit}}}\bigg|_{t=t_0}. \tag{19}$$

It is common practice to express the amount of a specific content in terms of its density parameter. In a flat Universe ($k = 0$) it follows that $\Omega_{\text{tot}} = \sum_i \Omega_i \equiv 1$.[8]

2.2.2 History of the Universe in a nutshell

The current understanding of our Universe's history tells the following story [11, 12]:

The Universe is born at the *Hot Big Bang* ($T = \infty$) after which it cools down while expanding rapidly. All four fundamental forces - the weak, strong, electromagnetic and gravitational force - are believed to be united initially. Quantum field theory and gravity might be unified by a *Theory of Everything* (TOE). We suspect that as the Universe evolved phase transitions in the early times might have 'split' it up: First, gravity was separated at about $T \sim 10^{19}$ GeV, then the GUT (*Grand Unified Theory*)-phase transition at $T \sim 10^{15}$ GeV might have brought up the electroweak and strong force. It was followed by a period of *inflation* in which the Universe expanded exponentially. Introduced as a possible solution to multiple cosmological problems[10] , it could not be proven to be correct until today. Next, we believe a *baryogenesis* mechanism to have taken place, which created an initial and very small quark-antiquark[11] asymmetry causing the large matter-antimatter asymmetry we observe today. At $T \sim 100$ GeV, the *electroweak phase transition* (EWPT) occurred, through which the SM particles received their mass via the Higgs mechanism. At that point, the electroweak gauge group $SU(2)_{\text{L}} \times U(1)_{\text{Y}}$ is broken down to $U(1)_{\text{EM}}$. A bit later at approximately $T \sim 100$ MeV, the *QCD-confinement phase trasition* took place at which quarks condensed to confined

---

[8]This follows from Eq. (17a): $H^2 = (8\pi G/3)\rho - k/a^2 \iff 1 - \Omega = -k/(aH)^2 \equiv 0$ if $k = 0$.

[9]Here, we mean the energy density generated by the cosmological constant Λ, $\epsilon_\Lambda = c^2\Lambda/8\pi G$.

[10]Explicitly, we want to name the flatness problem (*Why is the Universe (so) flat?*, the monopole problem (*Why don't we observe magnetic monopoles today?*) and the horizon problem (*Why is the CMB to uniform?*). For further explanations, see [11, 12].

[11]Antiparticles are denoted by a bar, e.g. $\bar{q}$.

bound states like mesons ($q\bar{q}$) (pions, kaons, etc.) or baryons (qqq) (protons, neutrons, etc.). After three minutes ($T \sim 100$ keV), the process of *Big Bang nucleosynthesis* (BBN) takes place - the first light nuclei were formed. Then, long after *matter-radiation equality* has been reached at $T \sim 0.75$ eV (see Fig. 4). Neutral hydrogen forms via $e^- + p^+ \rightarrow H + \gamma$ at *recombination* ($T \sim 0.26 - 0.33$ eV), letting the electron density decrease significantly. Following, *photons decouple*[12] at $T \sim 0.26$ eV as Thomson scattering $e^- + \gamma \rightarrow e^- + \gamma$ becomes more and more unlikely, resulting in the freely streaming *cosmic microwave background* (CMB) photons we observe today. After the CMB was born, the Universe found itself in a dark period that lasted until the first stars and galaxies formed. These were a new source of highly-energetical photons that re-ionized the matter content in the Universe. This stage is called *reionization* and might have happened around $T \sim 2.6 - 7.0$ meV. At matter–dark-energy equality ($T \sim 0.33$ meV), the Universe eventually entered the *dark era* that we are in today in which we observe an exponential expansion due to dark energy.
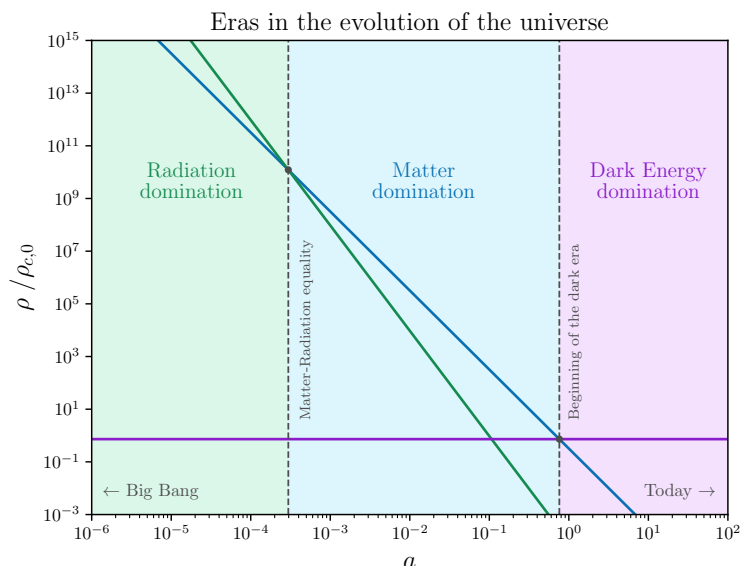

Figure 4: The three main eras in the history of the Universe.

---

[12]In a thermodynamic equilibrium, interactions (and their reversal) between particles are equally likely. As the temperature drops, one direction becomes favoured which results in the particles' leaving or *decoupling* from the equilibrium. Followingly, their number density *freezes-out*.

2.3 Cosmological phase transitions

As we have seen, phase transitions are key features in the cosmological evolution, especially in the early Universe. In the following section, we want to discuss their theoretical description.

2.3.1 Elements of statistical physics

A many-particle system is no longer described by its constitutents' individual motions but through macroscopic observables called *thermodynamic variables* such as its temperature T, pressure $\mathcal{P}$ and volume $\mathcal{V}$. In an equilibrium, these variables can be related to each other by a state function $f(T, \mathcal{P}, \mathcal{V}, N) = 0$. This relation spans a hypersurface in the phase space such that an equilibrium state corresponds to a point on this hypersurface - thus it is fully determined by the variables' values.

A crucial quantity in statistical physics is the *partition function $\mathcal{Z}$*, which corresponds to the number of all possible configurations of the system. All other important quantities can be derived from it (and its derivatives). Assuming the system is described by a canonical ensemble,[13] i.e. it is in contact with a thermal bath with which it transfers heat such that $\langle E \rangle$[14] = const. $\propto T$, the (Helmholtz) free energy F is given by

$$F = E - TS = -T \ln(\mathcal{Z}), \tag{20a}$$

$$f = \rho - Ts = -\frac{T}{\mathcal{V}} \ln(\mathcal{Z}). \tag{20b}$$

According to the Ehrenfest theorem, a statistical system undergoes a phase transition (PT) of nth order if the nth derivative of at least one thermodynamic potential, e.g. the free Energy $F(T, V, N)$, w.r.t. a thermodynamic variable, e.g. the temperature T, behaves in a discontinuous fashion when approaching a critical value for e.g. T. This special point is then called *critical temperature T_{c}*. However, a more modern classification distinguishes only between first-order (*discontinuous*) and second-order (*continuous*) PTs: The first-order PTs show a discontinuity at $T = T_{\text{c}}$ in the first derivative of e.g. the free energy F, and thus internal energy E as well. The energy gap separating the two phases from each other is called *latent heat* and is released during such a process. In contrast, at a second-order PT, $F^{(1)}(T \to T_{\text{c}})$ is finite, whereas $F^{(n>1)}(T \to T_{\text{c}})$ is discontinious or even divergent (for further details, see [13, 14]).

Sometimes it is also possible to parametrize this behaviour in terms of an *order parameter* that mirrors these discontinuities. This is of particular relevance in the case of first-order PTs resulting from SSB within a theory (for more details, see Section 2.3.3).

---

[13]In the case of the grand canonical ensemble, the system also exchanges also particles sucht that we have $\langle E \rangle$ = const., $\langle N \rangle$ = const. and $\Omega = -T \ln(\mathcal{Z})$, where Ω is the grand canonical potential.

[14]Here, $\langle \cdot \rangle$ represents the ensemble average.

2.3.2 Phase transitions in TQFT

In the framework of thermal quantum field theory (TQFT), the partition function $\mathcal{Z}$ can be expressed in the path integral formalism. Let us now consider the case of scalar field theory where the Lagrangian density $\mathcal{L}$ and the action $\mathcal{S}$ describing our physical system are functions of a scalar field ϕ. We can further perform a Fourier transform and decompose the field ϕ in the form $\phi \to \phi = \bar{\phi} + \phi'$, namely in its zero- and non-zero momentum modes,

$$\phi(x) = \int dp \, e^{ipx} \, \tilde{\phi}(p) = \underbrace{\int dp \, \delta(p) \, e^{ipx} \, \tilde{\phi}(p)}_{= \, \tilde{\phi}(P=0) \, \equiv \, \bar{\phi} \, = \, \text{const.}} + \underbrace{\int_{P \neq 0} dp \, e^{ipx} \, \tilde{\phi}(p)}_{= \, \phi'(x)} \quad (21)$$

$$= \bar{\phi} + \phi'(x).$$

In this decomposition, the partition function $\mathcal{Z}$ reads [15]

$$\mathcal{Z}(\mathcal{V}, T) = \exp\left(-\frac{\mathcal{V}}{T} \, f(T)\right) = \int_{-\infty}^{\infty} d\bar{\phi} \int_{P \neq 0} \mathcal{D}\phi' \, \exp\left[-\mathcal{S}_E(\phi = \bar{\phi} + \phi')\right] \quad (22)$$

$$= \int_{-\infty}^{\infty} d\bar{\phi} \, \exp\left[-\frac{\mathcal{V}}{T} V_{\text{eff}}(\bar{\phi})\right], \quad (23)$$

in which $f = F/\mathcal{V}$ is the free energy density, $\mathcal{S}_E = \int_X d^D x \, \mathcal{L}_E(\phi, \partial_\mu \phi)$ is the Euclidean action and $\mathcal{L}_E$ is the Euclidean Lagrangian density, where the transformation $t \to \tau = -it$ has been made.

Here we have introduced the concept of the *effective potential* V_{eff}. With its help, we can boil down the partition function $\mathcal{Z}$ to an integral over V_{eff} in which the integration variable is just the constant field $\bar{\phi}$. By looking at Eq. (23), we see that the integral will be dominated by the contribution that minimizes the exponent, i.e. the minimum of $V_{\text{eff}}(\bar{\phi})$. Therefore, we can expand the latter around its minimum[15],

$$V_{\text{eff}}(\bar{\phi}) \mid_{\bar{\phi} = \bar{\phi}_{\text{min}}} \approx V_{\text{eff}}(\bar{\phi}_{\text{min}}) + \frac{1}{2} V_{\text{eff}}''(\bar{\phi}_{\text{min}})(\bar{\phi} - \bar{\phi}_{\text{min}})^2, \quad (24)$$

and approximate the integral as follows:

$$\mathcal{Z}(\mathcal{V}, T) \approx \int_{-\infty}^{\infty} d\bar{\phi} \, \exp\left[-\frac{\mathcal{V}}{T}\left(V_{\text{eff}}(\bar{\phi}_{\text{min}}) + \frac{1}{2} V_{\text{eff}}''(\bar{\phi}_{\text{min}})(\bar{\phi} - \bar{\phi}_{\text{min}})^2\right)\right] \quad (25)$$

$$= \exp\left[-\frac{\mathcal{V}}{T} V_{\text{eff}}(\bar{\phi}_{\text{min}})\right] \cdot \underbrace{\int_{\infty}^{\infty} d\bar{\phi} \, \exp\left[-\frac{\mathcal{V}}{2T} V_{\text{eff}}''(\bar{\phi}_{\text{min}})(\bar{\phi} - \bar{\phi}_{\text{min}})^2\right]}_{\text{Gaussian integral}}$$

$$= \sqrt{\frac{2\pi T}{\mathcal{V} \cdot V_{\text{eff}}''(\bar{\phi}_{\text{min}})}} \, \exp\left[-\frac{\mathcal{V}}{T} V_{\text{eff}}(\bar{\phi}_{\text{min}})\right].$$

---

[15]Here, $V_{\text{eff}}'' = d^2 V_{\text{eff}}/d\phi^2$.

Thus, the free energy density $f = F/\mathcal{V}$ is approximately given as

$$f \stackrel{(20)}{=} -\frac{T}{\mathcal{V}} \ln(\mathcal{Z}) = V_{\text{eff}}(\bar{\phi}_{\text{min}}) - \frac{T}{2\mathcal{V}} \ln \left[\frac{2\pi T}{\mathcal{V} \cdot V_{\text{eff}}''(\bar{\phi}_{\text{min}})} \right] \xrightarrow{\mathcal{V} \to \infty} V_{\text{eff}}(\bar{\phi}_{\text{min}}). \tag{26}$$

In the thermodynamic limit $\mathcal{V} \to \infty$, the free energy density f is fully determined by the value of V_{eff} at its minimum $\bar{\phi}_{\text{min}}$. Its first derivative then reads

$$\frac{\partial f}{\partial T} = \frac{\partial V_{\text{eff}}(\bar{\phi}, T)}{\partial T} \bigg|_{\bar{\phi} = \bar{\phi}_{\text{min}}}. \tag{27}$$

▶ With all this knowledge, we can now conclude that a first-order PT occurs if the effective potential's derivative at its minimum, $\partial_T V_{\text{eff}}(\bar{\phi}, T)|_{\bar{\phi} = \bar{\phi}_{\text{min}}}$ is discontinuous! This is possible if $\bar{\phi}_{\text{min}} = \bar{\phi}_{\text{min}}(T)$ such that after crossing the critical temperature T_{c}, the effective potential develops a new second global minimum that is separated from the former one by a thermal potential barrier (see Section 2.3.3, 3). In this case, $\bar{\phi}_{\text{min}}(T)$ is the order parameter that characterized our phase transition. It corresponds to the vacuum expectation value (VEV) of the field $\bar{\phi}$, i.e. $\langle \bar{\phi}_{\text{min}} \rangle$. [16]

Calculating the effective potential V_{eff}. The exact expression of the effective potential V_{eff} is determined by the terms in the Langrangian density $\mathcal{L}_E$. To compute it explicitly, we have to evaluate

$$S_E(\phi = \bar{\phi} + \phi') = \int_0^{\beta = T^{-1}} d\tau \int_{\mathcal{V}} \mathcal{L}_E(\phi = \bar{\phi} + \phi') \tag{28}$$

$$= \int_0^{\beta = T^{-1}} d\tau \int_{\mathcal{V}} \mathcal{L}_E^{(0)}(\bar{\phi}) + \mathcal{L}_E^{(1)}(\bar{\phi}, \phi') + \ldots \tag{29}$$

$$= S_E^{(0)}(\bar{\phi}) + S_E^{(1)}(\bar{\phi}, \phi') + \ldots. \tag{30}$$

From Eq. (28) to Eq. (29), we sort the terms of $\mathcal{L}_E$ and collect them according to their order in ϕ'. Then, $\mathcal{L}_E^{(0)}(\bar{\phi})$ corresponds to the part independent of ϕ' (or only depending on $\bar{\phi}$), whereas $\mathcal{L}_E^{(1)}(\bar{\phi})$ contains the next (non-vanishing) higher order terms.[16]
We now want to show the remaining computation up to the first order: Comparing Eq. (22) with Eq. (23) and using Eq. (30), we obtain

$$\exp\left[-\frac{\mathcal{V}}{T} V_{\text{eff}}(\bar{\phi}) \right] = \int_{P \neq 0} \mathcal{D}\phi' \exp\left[-\left(S_E^{(0)}(\bar{\phi}) + S_E^{(1)}(\bar{\phi}, \phi') \right) \right] \tag{31}$$

$$= \underbrace{\exp\left(-S_E^{(0)}(\bar{\phi}) \right)}_{\equiv\, \exp\left(-\frac{\mathcal{V}}{T} V_{\text{eff}}^{(0)}(\bar{\phi}) \right)} \underbrace{\int_{P \neq 0} \mathcal{D}\phi' \exp\left(-S_E^{(1)}(\bar{\phi}, \phi') \right)}_{\equiv\, \exp\left(-\frac{\mathcal{V}}{T} V_{\text{eff}}^{(1)}(\bar{\phi}) \right)}. \tag{32}$$

---

[16]The terms linear in ϕ' are omitted because they will give no contribution since $\int dx\, \phi'(x) = \int dx\, \int_{P \neq 0} dp\, e^{ipx}\, \tilde{\phi}(p) = \int dx\, e^{ipx} \int_{P \neq 0} dp\, \tilde{\phi}(p) = \int_{P \neq 0} dp\, 2\pi\delta(p)\, \tilde{\phi}(p) = 0$.

We can now invert Eq. (32) for $V_{\text{eff}}(\bar{\phi})$. As a result, we eventually get the effective potential in form of an expansion in orders of $\bar{\phi}$, namely

$$V_{\text{eff}}(\bar{\phi}) \approx V_{\text{eff}}^{(0)}(\bar{\phi}) + V_{\text{eff}}^{(1)}(\bar{\phi}, T) + \ldots \tag{33}$$

$$= \underbrace{V_{\text{eff}}^{(0)}(\bar{\phi})}_{\text{Tree-level term}} + \underbrace{V_{\text{eff}}^{(1)}(\bar{\phi}, T = 0)}_{\text{vacuum 1-loop corr.}} + \underbrace{V_{\text{eff}}^{(1)}(\bar{\phi}, T)}_{\text{thermal 1-loop corr.}} . \tag{34}$$

The temperature dependence of the effective potential enters via the *thermal* 1-loop correction $V_{\text{eff}}^{(1)}(\bar{\phi}, T)$ that involves a *thermal integral* of the form [15]

$$J_T\left(\frac{m_{\text{eff}}}{T}\right) = \int_0^\infty dx' \, (x')^2 \, \ln\left[1 - \exp\left(-\sqrt{x^2 + y^2}\right)\right]\Big|_{y^2 = (m_{\text{eff}}/T)^2} \tag{35}$$

where $m_{\text{eff}} = m_{\text{eff}}(\bar{\phi} = 0) + m_{\text{eff}}(\bar{\phi})$ describes an *effective mass* that increases the 'naked' mass of the field in case of a non-vanishing field value. For later purposes, it is useful to expand (35) in terms of small or large $y = m_{\text{eff}}/T$, denoting the *high-temperature* and *low-temperature*[17] case [17], respectively:

$$J_T\left(\frac{m_{\text{eff}}}{T}\right) = \begin{cases} -\dfrac{\pi^2}{90} + \dfrac{1}{24}\left(\dfrac{m_{\text{eff}}}{T}\right)^2 - \dfrac{1}{12\pi}\left(\dfrac{m_{\text{eff}}}{T}\right)^3 + \ldots & y \to 0 : \text{High-T,} \\[4mm] -\left(\dfrac{m_{\text{eff}}}{2\pi T}\right)^{3/2} e^{-m_{\text{eff}}/T} + \ldots & y \to \infty : \text{Low-T} \end{cases} \tag{36}$$

---

[17]This is the well-known Boltzmann-distribution where $m \equiv m_{\text{eff}}(\bar{\phi})$.

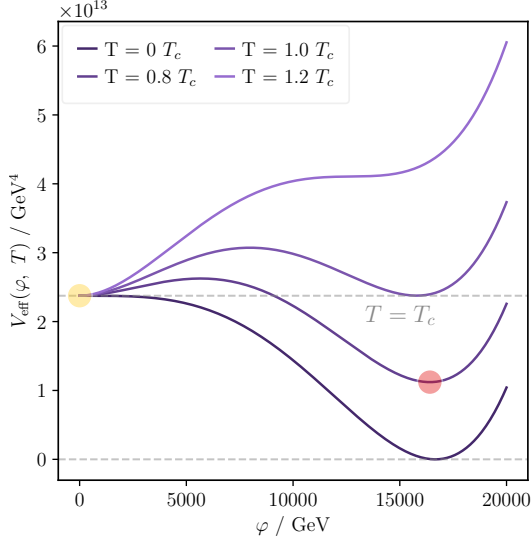### 2.3.3 How first-order PTs proceed: Bubble nucleation & growth

Figure 5: $V_{\text{eff}}(\varphi, T)$ for various T. Its temperature-dependent 1-loop corrections generate a second minimum (red dot) as T decreases.

We have learned that a first-order PT requires that the minimum of the effective potential, which is the VEV of the field φ, is a discontinuous function of the temperature, i.e. $\bar{\phi}_{\text{min}} \equiv \langle \varphi \rangle = \langle \varphi \rangle(T)$. This leaves us with the question: When and how is such a behaviour possible? First proposed in 1973, Coleman and Weinberg [18] presented a mechanism in which the *zero temperature* 1-loop contribution of the effective potential (see Eq. (34)) causes the SSB via the generation of a new global minimum. This will now be extended to the case where $T > 0$ by adding a thermal bath, i.e. the SM radiation bath in the early Universe.[18] The new *thermal* 1-loop contributions to the effective potential introduce its temperature dependence and will cause the following dynamics: At high temperatures $T \gg T_{\text{c}}$, the effective potential is dominated by the quadratic term in the high-temperature expansion of the *thermal* integral (36). It will only have one global minimum at $\varphi = 0$ such that $\langle \varphi \rangle = 0$. However, there exists a *critical temperature* T_{c} for which a second degenerate local minimum appears. For $T < T_{\text{c}}$, the second local minimum becomes the global one, representing the new energetically-favoured *true vacuum state* of the system where $\langle \varphi \rangle \neq 0$. The other minimum is then referred to as the *false vacuum state*. As can be seen in Fig. 5, both states are seperated by a thermal potential barrier below the critical temperature T_{c}. At $T = 0$, the false vacuum and thus the potential barrier disappears such that V_{eff} obstains the shape of a 'Mexican hat' potential.

▶ A *Cosmological phase transition* is then understood as a process in which the system (the Universe) transitions from the initial false to the true vacuum state. In the case of a first-order PT, the energy connected to the thermal potential barrier is then released and is called *latent heat*.

The semi-classical ansatz. The reason for such a PT to happen is that the false vacuum state is *metastable* such that a *decay rate* Γ can be associated with it. It is the key quantity to be computed in these kind of problems.

---

[18]We will later also refer to this as *primordial plasma*.

Originally, Calan and Coleman [19,20] developed the theory of the vacuum decay, which has been later extended to finite temperatures by Linde [21, 22]. Their approach of deriving the decay rate Γ is based on a *semi-classical ansatz*: The scalar's way from the false to the true vacuum is proceeding in two steps: First, overcoming the potential barrier by thermal $(T > 0)$ or quantum $(T = 0)$ fluctuations and arriving at an escape point φ_{init} with zero kinetic energy, and secondly, following the classical equations of motion from the escape point to the true vacuum. The latter is often referred to as *'rolling down the potential'*. The last stage of the process is characterized by the field oscillating around the global minimum, the true vacuum state. This *can* introduce a short matter dominated period since its energy density then scales as $\rho_\varphi \propto a^{-3}$. However, note that in the case of large friction, the escape point can also be in the true vacuum itself, meaning that there will be no significant oscillation and thus no matter dominated period (for further details, see Section 3.2).
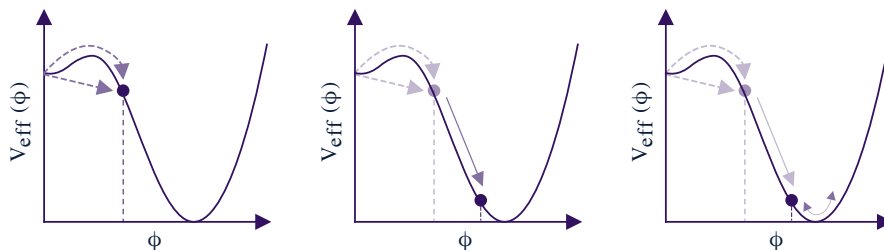

Figure 6: Scheme of the semi-classical theory that is used to describe the dynamics of a cosmological phase transition. *Left:* Thermal or quantum tunneling process from the false vacuum at $\varphi = 0$ to the escape point φ_{init}. *Middle:* The scalar field's 'rolling down the potential' movement, approaching the true vacuum at $\langle\varphi\rangle \neq 0$. *Right:* (Possible) oscillations of the scalar field around the true vacuum.

Let us now start with the explanation of the *tunneling* part: Following Coleman's (one-dimensional) particle analogy [19], let the Lagrangian of this problem be $L = \frac{1}{2}(\dot{q})^2 - V(q)$. The decay width associated with such a process is then given by $\Gamma \approx A \exp(-B/\hbar)$, where

$$B = 2 \int_{q_{\text{false}}}^{q_{\text{init}}} dq \ \sqrt{2V(q)} \equiv 2 \int_{q_{\text{false}}}^{q_{\text{init}}} dq \ \sqrt{2(E - V)}\Big|_{E=0} \tag{37}$$

should be integrated over the path for which B is minimal, i.e. $\delta B = 0$. Note that the solutions of the variation of the RHS of Eq. (37) are nothing else than the paths singled out by the Euler-Lagrange-equations with

$$\text{Real time:} \quad \frac{d^2q}{dt^2} = -\frac{dV}{dq}, \quad \frac{1}{2}\left(\frac{dq}{dt}\right)^2 + V = E = 0, \tag{38a}$$

$$\text{Imaginary time:} \quad \frac{d^2q}{d\tau^2} = +\frac{dV}{dq}, \quad \frac{1}{2}\left(\frac{dq}{d\tau}\right)^2 - V = E = 0. \tag{38b}$$

20

In Eq. (38a), we still have the negative sign at the potential's derivative. We can therefore apply a *first trick* and switch to the *imaginary time formalism* by performing $t \to \tau = it$, which results in the expression Eq. (38b). It is then possible to simply write $\delta B = \delta \int d\tau \; L_E = 0$ where $L_E = \frac{1}{2}(\partial_\tau q)^2 + V$ is the *Euclidean* Lagrangian (in imaginary time). The 'particle' travels from the false vacuum φ_{false} at $\tau = -\infty$ to the escape point φ_{init} at $\tau = 0$. The *second trick* is now to make use of the *time translation invariance* and re-adjust the particle's track such that it reaches the escape point at $\tau = 0$ coming from the false vacuum at $\tau = -\infty$, and *bounces* off and returns back to the latter at $\tau = +\infty$. This is why this particle trajectory is referred to as the *bounce solution* or *bounce*, for short. Combining Eq. (37) with these two tricks, this finally yields

$$\text{First trick:} \quad \int_{q_{\text{false}}}^{q_{\text{init}}} dq \; \sqrt{2V(q)} \equiv \int_{-\infty}^{0} d\tau \; L_E \tag{39}$$

$$\text{Second trick:} \quad \Rightarrow \quad B = 2 \int_{q_{\text{false}}}^{q_{\text{init}}} dq \; \sqrt{2V(q)} = \int_{-\infty}^{+\infty} d\tau \; L_E \equiv S_E, \tag{40}$$

where S_E is the *Euclidean* action (in imaginary time). Hence, the Euclidean action is directly involved in the decay rate Γ.

The good news is that we can directly translate this whole calculus to a four-dimensional scalar field theory version, where the path over which B is integrated is now the so-called *bounce* field configuration $\varphi(\tau, \mathbf{x})$, satisfying

$$\left(\frac{\partial^2}{\partial \tau^2} + \nabla^2 \right) \varphi = \frac{\partial V_{\text{eff}}(\varphi, T)}{\partial \varphi} \equiv V'_{\text{eff}}(\varphi, T) \tag{41}$$

in combination with the according boundary conditions

$$\text{a)} \; \lim_{\tau \to \pm\infty} \varphi(\tau, \mathbf{x}) = \varphi_{\text{false}}, \qquad \text{b)} \; \partial_\tau \varphi(\tau = 0, \mathbf{x}) = 0. \tag{42}$$

The first condition (a) states that at $\tau \to \pm\infty$, the field sits in the false vacuum, and the second one (b) reflects the fact that the field has no kinetic energy when arriving at the escape point at $\tau = 0$. It has been shown that the solution of Eq. (41) with the biggest contribution to S_E is rotationally symmetric in Euclidean space - it is O(4)-symmetric in the case of zero temperature and O(3)-symmetric in case of finite temperatures (see Linde [21, 22]). This means that the solution is only a function of r, i.e. $\varphi = \varphi(r)$ where $r = t^2 - \mathbf{x}^2$.[19] The equation of motion (41) then simplifies to

$$\frac{d^2\varphi}{dr^2} + \begin{cases} \dfrac{3}{r} \dfrac{d\varphi}{dr} = V'_{\text{eff}}(\varphi, T) & T = 0, \\[3mm] \dfrac{2}{r} \dfrac{d\varphi}{dr} = V'_{\text{eff}}(\varphi, T) & T \neq 0 \end{cases} \tag{43}$$

---

[19]We will often refer to r as the *radius* of the bubble (see next paragraph).

Since we are interested in examining processes in the early Universe, we will stick to the finite temperature version of Eq. (43). Hence, the final differential equation to be solved in our problem is

$$\frac{d^2\varphi}{dr^2} + \frac{2}{r}\frac{d\varphi}{dr} = V'_{\text{eff}}(\varphi, T), \tag{44a}$$

$$\lim_{r\to\pm\infty}\varphi(r) = 0, \quad \frac{d\varphi}{dr}\bigg|_{r=0} = 0. \tag{44b}$$

Henceforth, we call Eq. (44a) the *bounce equation*. It has to be solved numerically. A detailed description of the required methodology will be discussed in Section 4. Another consequence of working in the finite-T regime is that the Euclidean action reduces to its three-dimensional version, i.e. $S_4 = S_3/T$, in which S_3 is

$$S_3 = 4\pi \int dr\, r^2 \left[\frac{1}{2}\left(\frac{d\varphi}{dr}\right)^2 + \tilde{\Delta}V\right], \tag{45}$$

where $\varphi = \varphi(r)$ is the *bounce* yielding from Eq. (44a) and $\tilde{\Delta}V = V_{\text{eff}}(\varphi, T) - V_{\text{eff}}(\varphi_{\text{false}}, T)$. From longer calculations[20], one obtains the final form of the decay rate Γ per volume $\mathcal{V}$, namely [2]

$$\frac{\Gamma(T)}{\mathcal{V}} \simeq T^4 \left(\frac{S_3}{2\pi T}\right)^{\frac{3}{2}} \exp\left(-S_3/T\right). \tag{46}$$

▶ During the *tunneling process* (see Fig. 6) the field φ transitions form the false vacuum $\varphi_{\text{false}} \equiv 0$ to the escape point $\varphi_{\text{init}} \neq 0$. This *stochastic* procedure is characterized by the spherically (rotationally) symmetric *bounce* field configuration, also known as (*critical*) *bubble*. The process itself is then accordingly named *bubble nucleation*. From the T-dependence of Eq. (44a), it follows that $\varphi_{\text{init}} = \varphi_{\text{init}}(T)$ such that the critical bubble's profile will look differently for different *nucleation temperatures* T (see Fig. 7).

Notice that bubbles can only nucleate and grow successfully after some supercooling, i.e. the drop of the temperature below T_{c}, such that they experience an outward pressure $\Delta P \propto \Delta V \equiv V_{\text{eff}}(\varphi_{\text{false}}, T) - V_{\text{eff}}(\varphi_{\text{true}}, T) = V_{\text{eff}}(0, T) - V_{\text{eff}}(\varphi_{\text{true}}, T)$ due to the potential energy difference.

---

[20]The derivation of the decay rate's formula is rather complicated and lengthy such that we prefer to reference it: [15, 19, 21]. It requires a rather technical approach where one tries to find a non-trivial saddle point solution $\hat{\varphi}$ of the Euclidean action S_E that has at least one negative eigenvalue w.r.t. the deviation operator $\Delta \equiv \delta^2 S_E/\delta\varphi^2|_{\varphi=\hat{\varphi}}$. This will then induce an imaginary part in the free energy F which is in turn directly linked to the decay rate Γ.
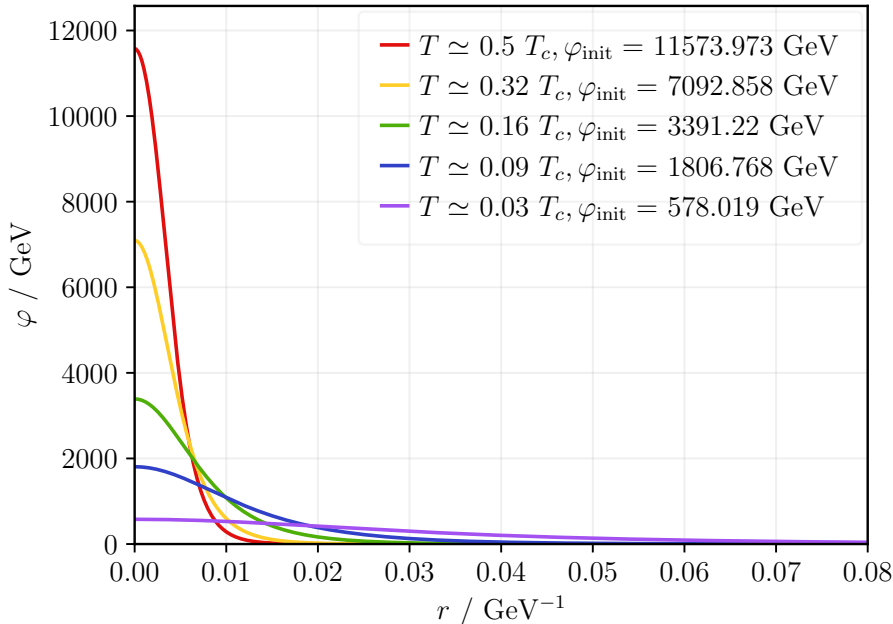
Figure 7: Bounces for various temperatures T. They interpolate between the escape point $\varphi(r = 0) = \varphi_{\text{init}}$ and the false vacuum $\varphi(r \to \infty) = \varphi_{\text{false}}$. The 'interpolation area' is also called *bubble wall*. As the temperature drops, the thermal potential barrier in $V_{\text{eff}}(\varphi, T)$ and thus φ_{init} decreases, while the bubble wall gets broader.

2.3.4 Gravitational waves from first-order cosmological PTs

In section 2.1.3, we have learned that non-vanishing spatial components of a source's energy-momentum tensor T_{ij} (see Eq. (14)) can induce gravitational waves. For this, we need anisotropic processes. Hence, the nucleation and expansion of spherically symmetric *bubbles* (see Eq. (44a) and Fig. 8) during a first-order PT does not generate GWs. However, the *collision* of such bubbles and its aftermath, e.g. *sound waves* and *turbulence* in the thermal radiation bath (*primordial plasma*) (see Fig. 9), can surely act as a source. In the following section, we want to give account of the most important quantities which can be used to model the resulting GW signal.

A remark on the computation of the GW spectrum. As can be seen in Fig. 7, bubbles that formed at different nucleation temperatures T_{n} will be unequally sized when they meet for collision. This process would generally have to be simulated on a spacetime lattice to keep track of every bubble's individual evolution. In fact, this was first done by Kosowsky, Turner and Watkins [23, 24]. They estimated the expected gravitational wave spectrum by computing T_{ij} from Eq. (14) in fully linearized GR and
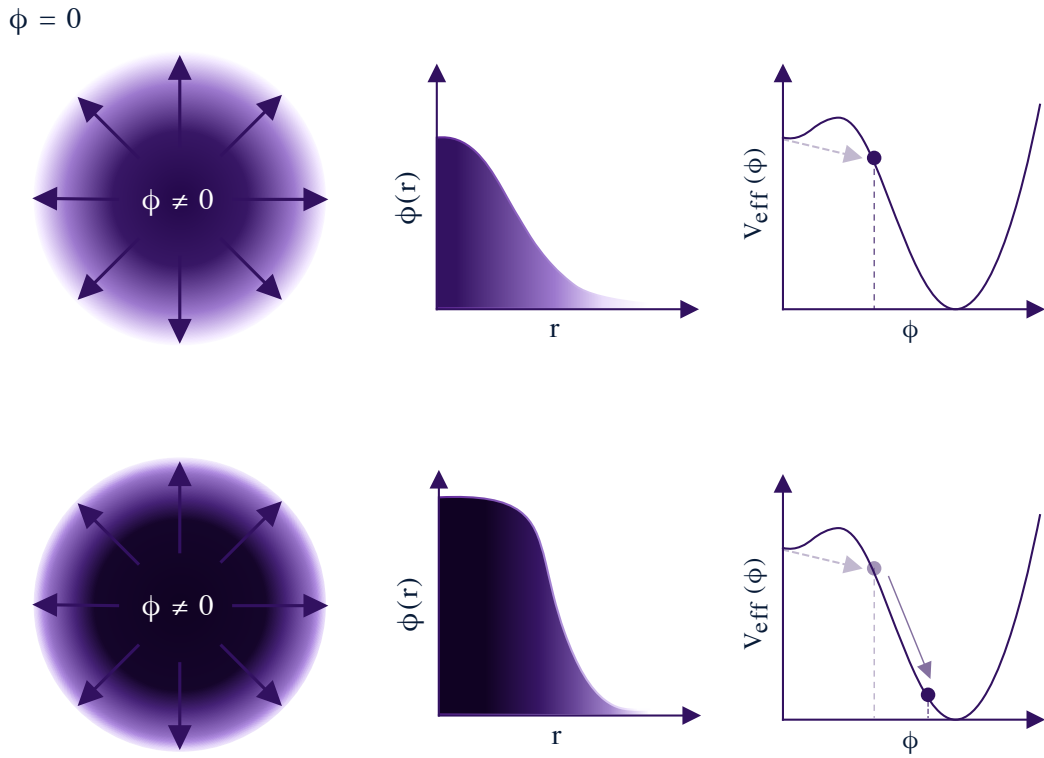
Figure 8: Scheme of bubble nucleation and growth during a first-order PT. *Top*: Nucleated bubble with initial profile. The latter corresponds to a '*thick-walled*' bubble, i.e. the field is still far away from the true vacuum state. *Bottom:* The same bubble at some later stage: The field ϕ has rolled down the potential and gets closer to the new true vacuum state. The bubble's wall profile approaches the look of a step function, it becomes more and more '*thin-walled*'.

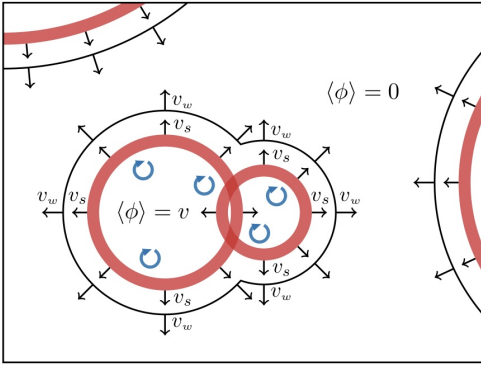Figure 9: The three major components of GW sources during a first-order PT: Bubble collisions (*black*), sound waves (*red*) and turbulences (*blue*). Despite the figure illustrating nicely the ongoing processes, it has one flaw: It is a simplification to say that the field value inside the bubble already corresponds the true vacuum at collision [16].

later on by introducing a new approximation called the *envelope approximation*.[21]: it neglects the intersection area of the colliding bubbles and thus excludes these regions from the spatial integration.

However, semi-analytical power law templates (see Eqs. (56), (57), (58)) for the GW spectrum in terms of $h^2\Omega_{\mathrm{GW}}(f)$ are also widely used to estimate the expected signal and are more convenient to use in our case. Hence, we will use the latter for our calculations. A remarkable result from the analysis of Kosowsky et al. is that the GW signal from a first-order PT only depends on a few gross feautures of the model and system under consideration: $T_\star$, α, κ, (β/H) etc.. The power law templates use exactly these characteristic quantities to parametrize the GW signal.

GW production and their characteristic quantities. The first question we have to answer is under which conditions bubble nucleation and growth are efficient in a rapidly expanding Universe. For that, two important quantities have to be compared to each other: the *decay rate per Hubble volume* Γ/H^3 from Eq. (46) and the *Hubble rate H* from Eq. (17a) (with $k = 0$ and $\rho \approx \rho_{\mathrm{vac}}$). If $\Gamma/H^4 < 1$, the expansion rate of the Universe is faster than the decay rate of the false vacuum. A collision of bubbles is very unlikely since they will be spatially separated from each other too quickly.. In contrast, if $\Gamma/H^4 \gtrsim 1$, the decay rate dominates the expansion rate such that the collision of bubbles can happen. We now define an *effective nucleation temperature* T_{n} of the bubbles as the solution of the equation $\Gamma(T = T_{\mathrm{n}}) = H^4(T = T_{\mathrm{n}})$ [25, 26]. If we assume that GW production happens instantaneously at bubble collision, we need to find a way to describe the collision time, or rather temperature. This is more difficult than it may appear, since we have collisions at multiple times. What is ordinarily done in the literature is considering the fraction of space being occupied by true vacuum state (bubbles). To do so, we can check the *probability to find a point still remaining in the*

---

[21]Note that in [23], they state that results produced by using the standard quadrupole approximation (see Eq. (14)) overestimated the gravitational wave spectrum compared to their results obtained by using full linearized GR.

unstable vacuum state $P(T) = \exp(-I(T))$, where the exponent $I(T)$ is given by [2]

$$I(T) = \frac{4\pi}{3} \int_T^{T_C} \frac{dT' \, \Gamma(T')}{(T')^4 H(T')} \left(\int_T^{\tilde{T}} \frac{d\tilde{T}}{H(\tilde{T})} \right)^3 , \tag{47}$$

involving the critical temperature T_c, the decay rate Γ from Eq. (46) and the Hubble parameter H now given explicitly by

$$H^2 = \frac{\rho_{\text{vac}} + \rho_{\text{rad}}}{3M_{\text{pl}}} = \frac{1}{3M_{\text{pl}}^2} \left(\Delta V(T) + \frac{\pi^2}{30} g_{\star,\varepsilon}(T) \, T^4 \right), \tag{48}$$

where ΔV is the potential energy difference between the two vacua [2]

$$\Delta V(T) = V_{\text{eff}} \left(\varphi_{\text{false}}(T), T \right) - V_{\text{eff}} \left(\varphi_{\text{true}}(T), T \right) \tag{49}$$
$$= V_{\text{eff}} \left(0, T \right) - V_{\text{eff}} \left(\varphi_{\text{true}}(T), T \right),$$

and $g_{\star,\varepsilon}(T)$ is the number of entropy degrees of freedom at temperature T. This integral has to be evaluated numerically, which is demonstrated in Section 4.

We then define[22] the temperature at which collisions (on average) happen as the fraction of space in the false vacuum is suppressed by $I(T = T_\star) = 0.34$ [2]. $T_\star$ is usually referred to as *percolation temperature*. In the following, all quantities with an index $\star$ are meant to be evaluated at $T = T_\star$. The bubble's average final radius at percolation $R_\star$ can be calculated via [2]

$$R_\star = \left[T_\star \int_{T_\star}^{T_c} \frac{dT'}{(T')^2} \frac{\Gamma(T')}{H(T')} \exp\left(-I(T') \right) \right]^{-\frac{1}{3}} \tag{50}$$

and is related to the *inverse PT duration* β [2] in terms of

$$\beta = (8\pi)^{\frac{1}{3}} (R_\star)^{-1}. \tag{51}$$

The tunneling process of the PT is followed by the release of latent heat, which will be converted partly into the kinetic energy of the accelerating bubble walls and will be partially used to heat up the thermal radiation bath. To quantify the fraction of energy released in each component, we first introduce the *transition strength* α as the ratio between the vacuum energy density and the energy density of the radiation bath,

$$\alpha(T) = \frac{\rho_{\text{vac}}(T)}{\rho_{\text{rad}}(T)} = \frac{\Delta V(T)}{(1/30) \, \pi^2 g_{\star,\varepsilon}(T) T^4} = \frac{30 \, \Delta V(T)}{\pi^2 g_{\star,\varepsilon}(T) T^4}. \tag{52}$$

For $\alpha > 1$, the (constant) vacuum energy density dominates the radiation bath energy density such that the Universe experiences exponential growth (*inflation*) until the scalar

---

[22]Note that in the literature there is no one straightforward way of defining the percolation temperature $T_\star$. Various conditions are used to estimate its value.s In [17, 26] for example, they use the condition: $I(T_\star) = 1 \Leftrightarrow P(T_\star) = 1/e$.

field φ starts to oscillate around the true vacuum state and behave like matter, i.e. $\rho_{\text{vac}} \propto a^{-3}$.

In the second step, it is useful to define the *efficiency factors* κ_{col} and κ_{SW}[23]for the conversion of the latent heat into the kinetic energy of the expanding bubble walls and the resulting sound waves in the primordial plasma. Following [2], these are given by

$$
\kappa_{\text{col}} = \frac{E_{\text{wall}}}{E_{\text{V}}} = \begin{cases} \left[1 - \frac{1}{3} \left(\frac{\tilde{\gamma}_{\star}}{\gamma_{\text{eq}}} \right)^2 \right] \left[1 - \frac{\alpha_{\infty}}{\alpha} \right], & \tilde{\gamma}_{\star} < \gamma_{\text{eq}}, \\ \frac{2}{3} \frac{\gamma_{\text{eq}}}{\tilde{\gamma}_{\star}} \left[1 - \frac{\alpha_{\infty}}{\alpha} \right], & \tilde{\gamma}_{\star} > \gamma_{\text{eq}}, \end{cases} \tag{53a}
$$

$$
\kappa_{\text{SW}} = \frac{\alpha_{\text{eff}}}{\alpha} \frac{\alpha_{\text{eff}}}{0.73 + 0.083\sqrt{\alpha_{\text{eff}}} + \alpha_{\text{eff}}}, \tag{53b}
$$

where we defined $\alpha_{\text{eff}} = \alpha \left(1 - \kappa_{\text{col}} \right)$, $\alpha_{\infty} \approx (1/24) \cdot 3 \, m_{Z'}^2 \, T_{\star}^2$ and introduced the bubble wall's Lorentz factor in equilibrium[24]and the ratio $\tilde{\gamma}_{\star}$ of the bubble's radius at nucleation and percolation [2],

$$
\gamma_{\text{eq}} = \sqrt{\frac{\Delta V - 0.04 \cdot 3 \, \Delta m^2 \, T_{\star}^2}{0.005 \cdot 3g^2 T_{\star}^4}}, \qquad \tilde{\gamma}_{\star} = \frac{2}{3} \frac{R_{\star}}{R_{\text{n}}} . \tag{54}
$$

A rough estimate of the duration of the observed sound wave period in the primordial plasma can be done by introducing the time scale $\tau_{\text{SW}} = R_{\star}/U_{\text{f}}$ after which the motion in the plasma becomes turbulent. Here, U_{f} is the root-mean square fluid velocity and is given by [2]

$$
U_{\text{f}} \simeq \sqrt{\frac{3 \, \alpha_{\text{eff}} \, \kappa_{\text{SW}}}{4 \, (1 + \alpha_{\text{eff}})}} . \tag{55}
$$

Semi-analytical power-law templates for Ω_{GW}. According to [2], the three contributions to the GW power spectral density (or *spectrum*) at percolation temperature $T_{\star}$ can be calculated by the following power-law templates involving the featured quantities:

   i Contribution from vacuum bubble collisions:

$$
\Omega_{GW,\star}^{\text{col}} = 2.30 \times 10^{-3} \, (R_{\star}H_{\star})^2 \left(\frac{\kappa_{\text{col}} \, \alpha}{1 + \alpha} \right)^2 \tag{56}
$$

$$
\times \left[1 + \left(\frac{f}{f_{\text{d}}} \right)^{-1.61} \right] \left(\frac{f}{f_{\text{col}}} \right)^{2.54} \left[1 + 1.13 \left(\frac{f}{f_{\text{col}}} \right)^{2.08} \right]^{2.30} ,
$$

---

[23]Sometimes an efficiency factor for the turbulence κ_{turb} is also introduced separately. However, we won't do that and will stick to the way it was handled in [2]: We simply relate the turbulence efficiency factor to the sound wave's one, as can be seen in its template in Eq. 58.

[24]Here, *in equilibrium* means that the pressure difference across the bubble wall is zero, see [2].

ii Contribution from sound waves in the primordial plasma:

$$\Omega_{GW,\star}^{\mathrm{sw}} = 0.384 \, (\tau_{\mathrm{SW}} H_\star) \, (R_\star H_\star) \tag{57}$$

$$\times \left(\frac{\kappa_{\mathrm{SW}} \, \alpha}{1+\alpha}\right)^2 \left(\frac{f}{f_{\mathrm{SW}}}\right)^3 \left[1 + \frac{3}{4}\left(\frac{f}{f_{\mathrm{SW}}}\right)^2\right]^{-\frac{7}{2}} ,$$

iii Contribution from turbulence in the primordial plasma:

$$\Omega_{GW,\star}^{\mathrm{turb}} = 6.85 \, (R_\star H_\star) \, (1 - \tau_{\mathrm{SW}} \, H_\star) \tag{58}$$

$$\times \left(\frac{\kappa_{\mathrm{turb}} \, \alpha}{1+\alpha}\right)^{\frac{3}{2}} \left(\frac{f}{f_{\mathrm{turb}}}\right)^3 \left[1 + \left(\frac{f}{f_{\mathrm{turb}}}\right)\right]^{-\frac{11}{3}} [1 + 8\pi f/H_\star]^{-1} .$$

The corresponding *peak frequencies*[25] of the GW spectra (and thus the signal) are related to the inverse radius of the bubble at percolation temperature,

$$f_{\mathrm{col}} = 0.28/R_\star, \quad f_{\mathrm{SW}} \simeq 3.4/R_\star, \quad f_{\mathrm{turb}} = 5.1/R_\star . \tag{59}$$

Lastly, the parameter $f_{\mathrm{d}} = 0.044/R_\star$ describes where the low-frequency slope of the GW spectrum changes.

Computation of the redshift factors. After their generation at $T_\star$, the GWs propagate through an evolving Universe which is undergoing different stages. Whenever a matter dominated period occurs, the GW spectrum will be redshifted and we have to scale it accordingly with a *redshift factor*. In our theory, it is possible that after percolation at $T = T_\star$, a *reheating* phase and thus an additional matter dominated phase takes place and lasts until some *reheating temperature* T_{RH} (for more details, see Section 3.2). The value of the latter is unknown and will be kept as a free parameter in our calculations. Recall that we generically express the energy density of gravitational radiation in terms of the Hubble parameter H and scale factor a, namely

$$\Omega_{\mathrm{GW}} = \frac{\rho_{\mathrm{GW}}}{\rho_{\mathrm{crit}}} = \frac{8\pi G}{3H^2} \, \rho_{\mathrm{GW}} \propto H^{-2} a^{-4} . \tag{60}$$

By using this relation, we can determine the amount of redshift after the GW has passed the additional reheating era and standard cosmological eras until today,

$$\Omega_{\mathrm{GW},0} = \Omega_{\mathrm{GW},\star} \times A_0 \times \left(\frac{a_\star}{a_{\mathrm{RH}}}\right)^4 \left(\frac{H_\star}{H_{\mathrm{RH}}}\right)^2 , \tag{61}$$

---

[25]When inserted into Eqs. (56), (57) and (58), we need to divide by $\hbar$ to go from GeV to Hz.

where $a_\star = a(T = T_\star)$, $a_{\mathrm{RH}} = a(T = T_{\mathrm{RH}})$, $H_{\mathrm{RH}} = H(T = T_{\mathrm{RH}})$ and A_0 is the total redshift factor from the end of reheating phase until today [2],

$$A_0 = \left(\frac{a_{\mathrm{RH}}}{a_0}\right)^4 \left(\frac{H_{\mathrm{RH}}}{H_0}\right)^2 \tag{62}$$

$$= 1.67 \times 10^{-5} h^{-2} \left(\frac{100}{g_{\star,\varepsilon}(T_{\mathrm{RH}})}\right)^{\frac{1}{3}} \left(\frac{a}{a_{\mathrm{RH}}}\right)^4 \left(\frac{H_{\mathrm{RH}}}{H_0}\right)^2 .$$

Note that in the case where no reheating and thus no additional matter dominated period occurs, i.e. $T_{\mathrm{RH}} = T_\star$, the last two factors in Eq. (61) will be equal to 1, such that we recover the GW spectrum expected with the standard cosmological history. For further
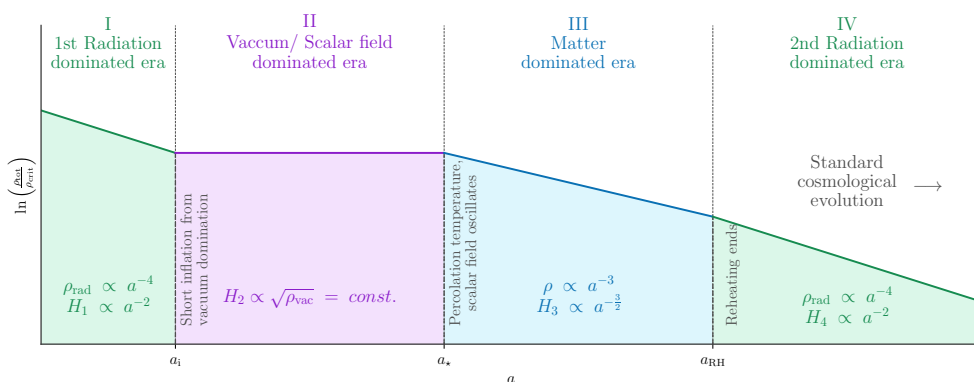

Figure 10: A modified cosmological evolution as a consequence of the Standard Model extension under consideration: In the middle of the standard radiation dominated epoch, we find a new vacuum (scalar field) and matter dominated era.

calculation, we need to check the scaling of H with a and T in the different epochs in our cosmic scenario as sketched in Fig. 10. Here, the index $i = 1, 2, 3, 4$ enumerates the corresponding epochs. The Hubble parameters are then given by

$$H_1(T) = H_4(T) \simeq \sqrt{\frac{\pi^2 \, g_{\star,\varepsilon}(T) \, T^4}{90 M_{\mathrm{pl}}^2}} \propto (a(T))^{-2}, \tag{63}$$

$$H_2(T) \simeq \sqrt{\frac{\Delta V(T)}{3 M_{\mathrm{pl}}^2}} = \text{const.}, \quad H_3(T) \propto (a(T))^{-3/2} . \tag{64}$$

We match their values at $T_\star$ and T_{RH} by imposing two continuity conditions,

$$H_2(T = T_\star) \stackrel{!}{=} H_3(T = T_\star) \tag{65a}$$

$$H_3(T = T_{\mathrm{RH}}) \stackrel{!}{=} H_4(T = T_{\mathrm{RH}}) . \tag{65b}$$

From this, we obtain the following relations:

$$H_3(T) = H_3(T_\star) \times \left(\frac{a_\star}{a}\right)^{\frac{3}{2}} \overset{(65\text{a})}{=} H_2(T_\star) \times \left(\frac{a_\star}{a}\right)^{\frac{3}{2}}, \tag{66a}$$

$$H_4(T) = H_4(T_{\text{RH}}) \times \left(\frac{a_{\text{RH}}}{a}\right)^2 \overset{(65\text{b})}{=} H_3(T_{\text{RH}}) \times \left(\frac{a_{\text{RH}}}{a}\right)^2 \tag{66b}$$

$$= H_2(T_\star) \times \left(\frac{a_\star}{a_{\text{RH}}}\right)^{\frac{3}{2}} \times \left(\frac{a_{\text{RH}}}{a}\right)^2$$

$$\Rightarrow H_{\text{RH}} = H_4(T_{\text{RH}}) = H_2(T_\star) \times \left(\frac{a_\star}{a_{\text{RH}}}\right)^{\frac{3}{2}}. \tag{66c}$$

Lastly, the factor $(a_\star/a_{\text{RH}})$ can be found via

$$H_{\text{RH}} = H_2(T_\star) \times \left(\frac{a_\star}{a_{\text{RH}}}\right)^{\frac{3}{2}} \overset{!}{=} \sqrt{\frac{\rho_{\text{rad}}(T_{\text{RH}})}{3M_{\text{pl}}}} \overset{(63)}{=} \sqrt{\frac{\pi^2 \, g_{\star,\varepsilon}(T_{\text{RH}}) \, T_{\text{RH}}^4}{90M_{\text{pl}}^2}}, \tag{67}$$

$$\Rightarrow \left(\frac{a_\star}{a_{\text{RH}}}\right) = \left[\frac{\pi^2 \, g_{\star,\varepsilon}(T_{\text{RH}}) \, T_{\text{RH}}^4}{30 \, \Delta V(T_\star)}\right]^{\frac{1}{3}}. \tag{68}$$

Finally, the total redshift factor for the GW energy density reduces to

$$\Omega_{\text{GW,RH}} = \Omega_{\text{GW},\star} \times A_0 \times \left(\frac{a_\star}{a_{\text{RH}}}\right)^4 \left(\frac{H_\star}{H_{\text{RH}}}\right)^2 \tag{69}$$

$$= \Omega_{\text{GW},\star} \times A_0 \times \left(\frac{a_\star}{a_{\text{RH}}}\right)^4 \left(\frac{H_2(T_\star)}{H_2(T_\star)\left(\frac{a_\star}{a_{\text{RH}}}\right)^{\frac{3}{2}}}\right)^2$$

$$= \Omega_{\text{GW},\star} \times A_0 \times \left(\frac{a_\star}{a_{\text{RH}}}\right) = \Omega_{\text{GW},\star} \times A_0 \times \left[\frac{\pi^2 \, g_{\star,\varepsilon}(T_{\text{RH}}) \, T_{\text{RH}}^4}{30 \, \Delta V(T_\star)}\right]^{\frac{1}{3}}.$$

The peak frequencies of the GW spectra as well as f_{d} will also shift accordingly while the Universe expands: it scales like $f \propto a^{-1}$. Using the relation from entropy conservation,

$$g_{\star,\varepsilon}(T)T^3a^3 = \text{const.} \quad \Rightarrow \quad a \propto \left(g_{\star,\varepsilon}(T) \, T^3\right)^{-\frac{1}{3}}, \tag{70}$$

we find the following behaviour:

$$f_0 = f_\star \times \left(\frac{a_\star}{a_{\text{RH}}}\right) \times \left(\frac{a_{\text{RH}}}{a_0}\right) \tag{71}$$

$$= f_\star \times \left[\frac{\pi^2 \, g_{\star,\varepsilon}(T_{\text{RH}}) \, T_{\text{RH}}^4}{30 \, \Delta V(T_\star)}\right]^{\frac{1}{3}} \times \left(\frac{g_{\star,\varepsilon}(T_0)}{g_{\star,\varepsilon}(T_{\text{RH}})}\right)^{\frac{1}{3}} \times \left(\frac{T_0}{T_{\text{RH}}}\right),$$

30

where T_0 is the thermal radiation bath's present temperature, i.e. the temperature of the CMB, $T_0 = T_{CMB} = 2.725$ K $= 2.725 \times 8.62 \times 10^{-14}$ GeV.

▶ The total GW spectrum we would measure today amounts to the sum of the three contributions (see Eqs. (56), (57), (58)) that we multiply by the redshift factor $(a_\star/a_{RH})$ from Eq. (68) and A_0 from Eq. (62),

$$\Omega_{GW} \equiv \Omega_{GW,0}^{tot} = A_0 \times \left(\frac{a_\star}{a_{RH}}\right) \times \left[\Omega_{GW}^{col,\star} + \Omega_{GW}^{sw,\star} + \Omega_{GW}^{turb,\star}\right] . \tag{72}$$

Signal-to-noise ratio ρ. After having calculated the expected GW spectrum, the final question to ask is: Are we even able to detect the signal with present or future observatories? Intuitively, the GW signal must exceed the noise that is registered by the detector. Hence, the exact answer depends on the technical features of the experiment, such as the observation time t_{obs}, the frequency range $[f_{min}, f_{max}]$ and the various noise sources. A scalar quantity which unifies all these aspects is the so-called *signal-to-noise ratio* (SNR). In the case of a stochastic gravitational wave background as from cosmological phase transitions, we need to consider the auto-correlated SNR for a single detector, which reads [8]

$$\rho^2 = t_{obs} \int_{f_{min}}^{f_{max}} df \left[\frac{h^2 \Omega_{GW}(f)}{h^2 \Omega_{eff}(f)}\right]^2 . \tag{73}$$

Clearly, we compute the SNR by computing the overlap of the curves from the expected GW spectrum $h^2 \Omega_{GW}$ and from the sum of all noise sources, which is converted back to an *effective GW power spectral density* $h^2 \Omega_{eff}$ (or *effective GW spectrum*). The latter will be specific to the detector under consideration. Coming back to the originally posed question, the GW signal will be detectable if the corresponding SNR is greater than the detector-specific threshold value ρ_{thr}.

In this work, we calculate the SNR for the upcoming LISA experiment, which is planned to launch in 2034 [8, 27, 28]. The corresponding experimental data are given in Table 1. The effective GW spectrum $h^2 \Omega_{eff}$ for LISA can be calculated with [8]

$$\Omega_{GW}^{eff}(f) = \frac{2\pi^2}{3H_0^2} f^3 S_{LISA}^{eff}(f) \tag{74}$$

$$\Leftrightarrow \quad h^2 \Omega_{GW}^{eff}(f) = \frac{2\pi^2}{3} \times \left(100 \times \frac{km \ Hz}{Mpc}\right)^{-2} \times f^3 S_{LISA}^{eff}(f) \tag{75}$$

$$= \frac{2\pi^2}{3} \times \left(3.0857 \times 10^{17}\right)^2 \times f^3 S_{LISA}^{eff}(f) \ Hz^{-2} , \tag{76}$$

31

where we have used the Hubble parameter H_0 at present time,

$$H_0 = 100 \times h \times \frac{\text{km Hz}}{\text{Mpc}} = 100 \times h \times \frac{10^3 \text{ m}}{3.0857 \times 10^{19} \times 10^3 \text{ m}} \text{ Hz} \qquad (77)$$

$$= \frac{h}{(3.0857 \times 10^{17})} \text{ Hz} \qquad (78)$$

The *noise strain power spectral density* $S_{\text{LISA}}^{\text{eff}}$ reads [8]

$$S_{\text{LISA}}^{\text{eff}} = \frac{10}{3L^2} \left(P_{\text{OMS}}(f) + 2 \left[1 + \cos^2\left(\frac{f}{\tilde{f}}\right) \right] \frac{P_{\text{acc}}(f)}{(2\pi f)^4} \right) \qquad (79)$$

$$\times \left[1 + \frac{6}{10} \left(\frac{f}{f_\star}\right)^2 \right] + S_c(f),$$

where $\tilde{f} = c/(2\pi L)$ is the so-called transfer frequency and $L = 2.5 \times 10^9$ m is the length of LISA's interferometer arms. Eq. (79) is composed of the experiment's several noises [8], such as the optical metrology noise

$$P_{\text{OMS}}(f) = (1.5 \times 10^{-11} \text{ m}^2)^2 \left[1 + \left(\frac{2 \text{ mHz}}{f}\right)^4 \right] \text{ Hz}^{-1}, \qquad (80)$$

the test mass acceleration noise

$$P_{\text{acc}}(f) = (3 \times 10^{-15} \text{ ms}^{-2})^2 \left[1 + \left(\frac{0.4 \text{ mHz}}{f}\right)^2 \right] \left[1 + \left(\frac{f}{8 \text{ mHz}}\right) \right] \text{ Hz}^{-2}, \qquad (81)$$

and the noise from unresolved galactic binaries after 4 years

$$S_c(f) = 9 \times 10^{-45} \left(\frac{f}{\text{Hz}}\right)^{-\frac{7}{3}} \exp\left[-\left(\frac{f}{\text{Hz}}\right)^{0.138} - 211 \left(\frac{f}{\text{Hz}}\right) \sin\left[521 \left(\frac{f}{\text{Hz}}\right) \right] \right]$$

$$\times \left\{ 1 + \tanh\left[1680 \left(0.0013 - \left(\frac{f}{\text{Hz}}\right) \right) \right] \right\} \text{ Hz}^{-1}. \qquad (82)$$

3 The Model:
Classical Conformal B − L Extension of the Standard Model of particle physics

Stochastical gravitational waves can be generated by cosmological phase transitions of first-order, which are unfortunately not included in the current repertoire of the Standard Model (SM). However, one could try to think of some extension of the SM with a suitable mechanism such that this becomes possible. Following Coleman's and Weinberg's [18] idea of spontaneous symmetry breaking via *loop* corrections, we want to investigate a common SM extension where precisely such a mechanism enables a first order PT [29].

3.1 The setup

In the *classical conformal* B − L *extension*, we promote the global $U(1)_{\mathrm{B-L}}$-symmetry of the SM to a new local gauge symmetry. Here, by B − L we mean the difference between the baryon number B and lepton number L. This theory comes with a new complex scalar field $\phi = (\varphi + iG)/\sqrt{2}$ with its physical field φ and Goldstone boson G^{26}, a gauge boson Z' and three right-handed neutrinos ν_{R}^i. However, we will follow the simpler approach from [1, 2] and consequently not consider the fermionic contributions.

In this model, the Lagrangian density $\mathcal{L}$ [30] reads

$$\mathcal{L} = \mathcal{L}'_{SM} - \frac{1}{4}Z'_{\mu\nu}Z'^{\mu\nu} + |D_\mu\phi|^2 - V(H, \phi). \tag{83}$$

First, we have the SM Lagrangian density $\mathcal{L}'_{SM}$, where the prime denotes the exclusion of the (relevant) Higgs-related terms. The second term represents the kinetic part of the vector field Z'_μ corresponding to the new Z'-boson. The according field strength tensor $Z'_{\mu\nu}$ is defined as

$$Z'_{\mu\nu} = \partial_\mu Z'_\nu - \partial_\nu Z'_\mu. \tag{84}$$

Furthermore, we add the square of the covariant derivative,

$$D_\mu\phi = \left(\partial_\mu + i2gZ'_\mu\right)\phi, \tag{85}$$

which includes the scalar's kinetic term and interaction term with the Z'-boson via the gauge coupling $g \equiv g_{\mathrm{B-L}}$. The last term is the potential,

$$V(H, \phi) = \lambda_{\mathrm{H}}(H^\dagger H)^2 + \lambda_{\mathrm{H}\phi}(H^\dagger H)(\phi^\dagger\phi) + \lambda_\phi(\phi^\dagger\phi)^2, \tag{86}$$

that introduces a portal coupling between the new complex scalar ϕ and the SM Higgs doublet H. Here, $\lambda_\phi, \lambda_{\mathrm{H}} > 0$ represent the self-couplings for the Higgs and scalar field,

---

[26]It is well-known that the Goldstone boson G is gauge dependent and thus yields no physical particle: by using a local U(1)-transformation with a specific choice of $\alpha(x)$, we can get rid of G and obtain $\phi \equiv \varphi \in \mathbb{R}$ as a result [29]. Henceforth, we will identify ϕ with its physical field φ.

Particle	Effective mass $m_i^2(\varphi)$	Debye mass $\Pi_i(T)$	dofs n_i	c_i
φ	$3\lambda_0\varphi^2$	$\left(g^2 + \lambda_0/3\right)T^2$	1.0	3/2
G	$\lambda_0\varphi^2$	$\Pi_\varphi(T)$	1.0	3/2
Z'	$4g^2\varphi^2$	$4g^2T^2$	3.0	5/6

Table 3: The main ingredients of our SM extension and their properties.

respectively, and $\lambda_{\mathrm{H}\phi} < 0$ is the interaction coupling between the latter. Note that the dimensionful mass term $\propto \mu^2\left(H^\dagger H\right)$ of the standard Higgs-potential has been replaced by an interaction term $\propto \lambda_{\mathrm{H}\phi}(H^\dagger H)(\phi^\dagger\phi)$ between the new complex scalar ϕ and the Higgs H. This feature goes hand in hand with the model's *classical conformality* – there is no dimensionful scale appearing in the (effective) potential at tree-level. As a consequence, the Higgs mass will be dynamically generated as soon as the scalar ϕ aquires its non-zero VEV.

The corresponding 1-loop effective potential (in the φ-direction)[27] [30, 31] is

$$V_{\mathrm{eff}}(\varphi, T) \;=\; V_{\mathrm{eff}}^{(0)}(\varphi) + V_{\mathrm{eff}}^{(1)}(\varphi, T) \; + V_{\mathrm{daisy}}(\varphi, T) \tag{87}$$

where the single contributions are

$$V_{\mathrm{eff}}^{(0)}(\varphi) \;=\; \frac{1}{4}\lambda_0\varphi^4 \tag{88}$$

$$V_{\mathrm{eff}}^{(1)}(\varphi, T) \;=\; V_{\mathrm{CW}}(\varphi) + \frac{T^4}{2\pi^2}\sum_i k_i J_T\left(m_i^2(\varphi)\right), \tag{89}$$

$$V_{\mathrm{daisy}}(\varphi, T) \;=\; -\sum_j \frac{T}{12\pi}\left[\left(m_j^2(\varphi) + \Pi_j(T)\right)^{\frac{3}{2}} - \left(m_j^2(\varphi)\right)^{\frac{3}{2}}\right]. \tag{90}$$

Here, the summation is performed over all particle species under consideration, $i, j \in \{\varphi, Z', G\}$. The zero-temperature 1-loop correction of the effective potential is the *Coleman-Weinberg potential* [30],

$$V_{\mathrm{CW}} = \sum_i \frac{k_i m_i^4(\varphi)}{64\pi^2}\left[\ln\left(\frac{m_i^2(\varphi)}{\bar{\mu}^2}\right) - c_i\right], \tag{91}$$

where k_i is the particle's number of degrees of freedom (dofs), $m_i(\varphi)$ is its effective mass, $\bar{\mu}$ is the renormalization scale[28] and c_i is a species dependent constant (see Table 3.1). Note that we fix the coupling λ_0 in the quartic tree-level term in such a way that the only

---

[27]We want to focus on investigating the symmetry breaking in the $(\phi, h = 0)$-direction. More details can be found in Section 3.2.

[28]Here, we chose $\bar{\mu}$ to be the value of the zero-temperature VEV $\langle\varphi\rangle_0$ of ϕ [2].

free parameters of the model, g and $m_{Z'}$, can be related to each other via $m_{Z'} = 2g\langle\varphi\rangle_0$, where $\langle\varphi\rangle_0$ is the zero-temperature VEV of φ. This lets us explore the model within the parameter space that is spanned by g and $m_{Z'}$. The *thermal* 1-loop correction involves the typical temperature integral as seen in Eq. (35), where k_i is the particle's number of dofs and T is the temperature. Lastly, we have the temperature-dependent term from the *daisy resummation*[29] including the *thermal* or *Debye masses* $\Pi_i(T)$, which have to be considered to face the problem of divergencies.
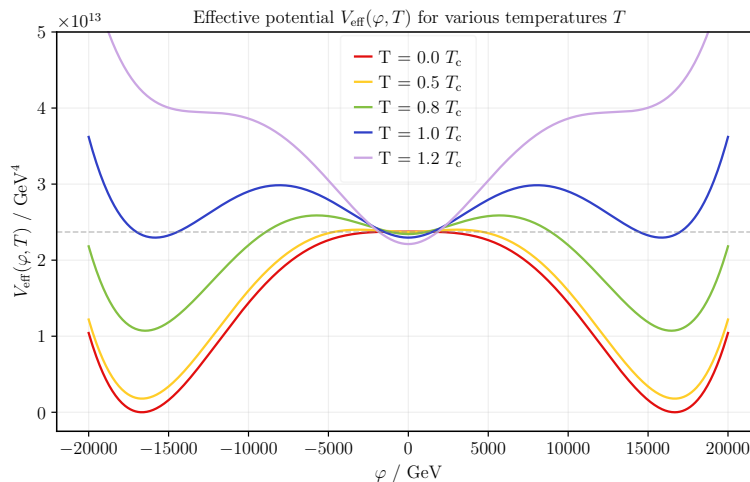

Figure 11: Effective potential $V_{\text{eff}}(\varphi, T)$ up until 1-loop correction plotted for the model parameters $g = 0.3$ and $m_{Z'} = 10^4$ GeV. The degeneracy of the minima at $T = T_{\text{c}}$ is shown by the grey dotted line.

The core of this model is the $U(1)_{\text{B}-\text{L}}$ symmetry breaking caused by the *zero-temperature* 1-loop corrections [18] (see Eq. (91)) in the φ-direction of the effective potential V_{eff}. The additional *thermal* 1-loop corrections (see second term in Eq. (89)) introduces a temperature dependence for the potential's minimum and induces a thermal potential barrier, which enables a first-order phase transition below the critical temperature $T_{\text{c}} = T_{\text{c}}(g, m_{Z'})$ (see Section 2.3). As can be seen in Fig. 3.1, at high temperatures, $T \gg T_c$, the high-T expansion from Eq. (36) tells us that the quadratic term is dominant. Thus we only expect the effective potential to have one global minimum at $\varphi = 0$. By lowering the temperature, we arrive at $T = T_{\text{c}}$, where a degeneracy occurs due to the appearance of a second local minimum. After crossing this temperature threshold, the second local minimum deepens and becomes the new global minimum representing the new energetically-favoured true vacuum state (the new *VEV*). In our model, it is separated from the false vacuum state at $\varphi = 0$ by a thermal potential barrier which

---

[29]These terms do not originate from the procedure described in Section 2.3.2. They are separately introduced to handle the divergencies. See [31] for further details.

exists up until $T \to 0$. This enables the occurence of a supercooled first-order PT well below the critical temperature $T \ll T_\mathrm{c}$ (see Section 2.3 for detailed process description).

As soon as $T = T_\mathrm{c}$, the field aquires a new non-zero VEV $\langle \varphi \rangle$ which leads to the breakdown of the $U(1)_{\mathrm{B-L}}$-symmetry. To see this explicitly, consider a reparametrization of the field φ of the form

$$\varphi \to \varphi = \bar{\varphi} + \langle \varphi \rangle(T) \quad \text{with} \quad \langle \varphi \rangle(T) = \begin{cases} 0, & T > T_\mathrm{c}, \\ \neq 0, & T \leq T_\mathrm{c}, \end{cases} \tag{92}$$

where $\bar{\varphi}$ represents the physical field and the VEV $\langle \varphi \rangle(T)$ acts like a constant[30] background field. We can reinsert this now into the models's Lagrangian density from Eq. (83) and use this to study its symmetry behaviour:
Above the critical temperature T_c, all the terms are still invariant under the corresponding symmetry transformations. We have simply renamed φ to $\bar{\varphi}$. For $T \leq T_\mathrm{c}$, the VEV becomes non-zero and new terms appear from the covariant derivative from Eq. (85),

$$|D_\mu(\bar{\varphi} + \langle \phi \rangle)|^2 = \underbrace{(\partial_\mu \bar{\varphi})^2}_{\text{kinetic term of } \bar{\varphi}} + \underbrace{4g^2 \langle \phi \rangle^2 Z'_\mu Z'^\mu}_{\text{new mass term of } Z'} \tag{93}$$
$$+ \underbrace{4g^2 (Z'_\mu \, \bar{\varphi})(Z'^\mu \, \bar{\varphi})}_{\text{interaction term between } \bar{\varphi} \text{ and } Z'}$$

such that the *new* Lagrangian density $\mathcal{L}_{\mathrm{T} < \mathrm{T_c}}$ below the critical temperature is

$$\mathcal{L}_{\mathrm{T} < \mathrm{T_c}} = \mathcal{L}_{\mathrm{T} > \mathrm{T_c}} + 4g^2 \langle \varphi \rangle^2 Z'_\mu Z'^\mu. \tag{94}$$

One can see that the Z'-boson acquires its mass when $\langle \phi \rangle$ becomes non-zero. The new Z'-mass term is not invariant under the $U(1)_{\mathrm{B-L}}$-symmetry transformations.[31] Followingly, the whole Lagrangian density $\mathcal{L}$ (83) is no longer symmetric and thus, the $U(1)_{\mathrm{B-L}}$-symmetry has been spontaneously broken.

---

[30]Here, *constant* means not spacetime-dependent.
[31]Symmetry transformations with regards to a U(1)-symmetry are i) for scalars: $\phi \to \phi' = e^{i\alpha(x)}\phi$, and ii) for vectors and $A_\mu \to A'_\mu = A_\mu - \frac{1}{qg}(\partial_\mu \alpha(x))$.

3.2 Cosmological scenarios

Let's consider this mechanism in the context of cosmology and the history of the early Universe: Suppose we start in the radiation dominated era where the field 'sits' initially in the false vacuum, i.e. $\varphi = \langle \varphi \rangle = 0$. The modified cosmological history will now depend on the temperature scales in our model: The *percolation temperature* $T_\star$ and the *inflationary temperature* T_i at which the scalar field's energy density (or *vacuum* energy density) is equal to the radiation bath energy density, i.e. $\alpha(T = T_i) = 1$. We can now distinguish several possible cases, which can be studied with Fig. 12:

i $T_\star > T_i$ (left, grey): The vacuum energy density doesn't dominate the radiation energy density of the thermal bath at percolation. Hence, there can be neither a thermal inflation nor a reheating and matter dominated phase. We simply recover the case of the standard cosmological evolution.

ii $T_\star < T_i$ (right, lavender): In this case, the vacuum energy density dominates the one of the thermal radiation bath, causing a short thermal inflation period which is assumed to stop at $T_\star$. Consequently, a way of transferring this vacuum energy back to the SM thermal radiation bath is necessary. Depending on the amount of friction a bubble experiences, there will be two further ways:

– If the friction across the bubble wall is great (left, grey), the vacuum energy will be transferred instantaneously to the thermal radiation bath. The result is a scalar field which does not oscillate such that no matter dominated era emerges. Thus, we effectively have $T_{RH} = T_i$.

– If the friction is small (right, blue), a large amount of vacuum energy will be left, such that the scalar field will oscillate around the true vacuum state, yielding a matter dominated era. This way it transfers energy via decays into SM particles during the *reheating phase* which ends at $T_{RH} \leq T_i$. After this phase, the symmetries will be restored again and the standard evolution will continue.

▶ Due to the conformal nature of this model, the percolation temperature $T_\star$ may lie well below the critical temperature T_c. This results in the scalar field φ being trapped in the false vacuum, yielding a vacuum dominated eraas the driving force of a thermal inflation. We therefore expect a reheating phase and matter-dominated era to happen in which the scalar oscillate. This pathway corresponds to the solid black line in Fig. 12.
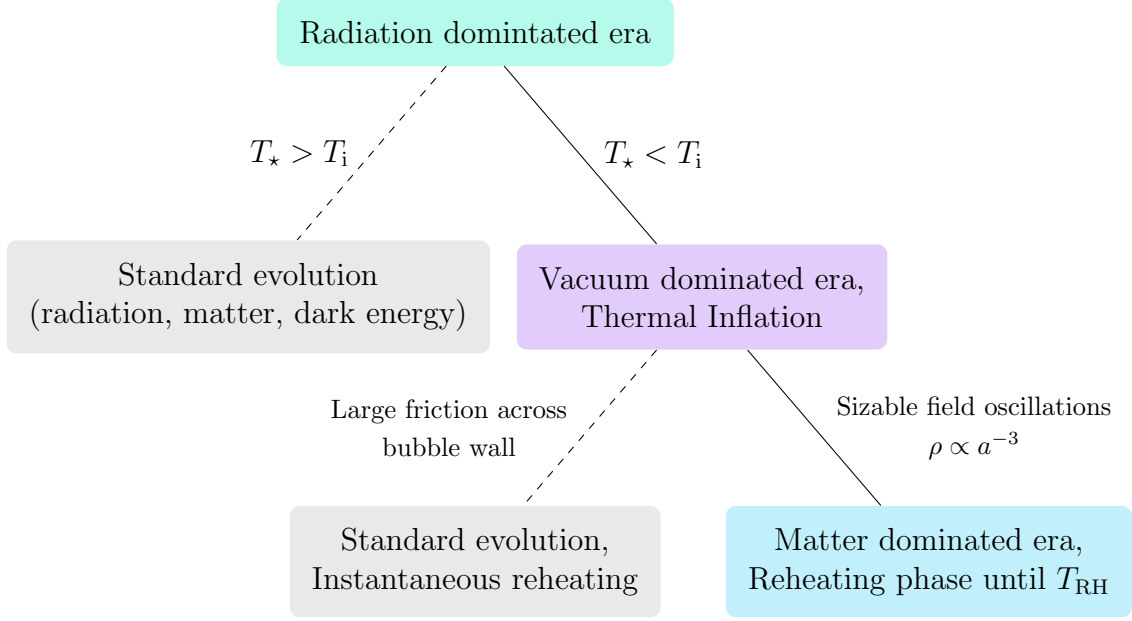
Figure 12: Possible modified cosmological trajectories in the B − L-extended SM. The solid line trajectory is also sketched in terms of the evolution of the energy density with the scale factor in Fig. 10.

Depending on whether the temperature $T_\star$ at which the B − L-PT ends is higher or lower than $T_{\mathrm{QCD}} \sim 100$ MeV, we expect two different chronologies that involve first-order PTs:

First-order $(B − L)$-PT. For $T_\star > T_{\mathrm{QCD}}$, the $(B − L)$-PT is of first-order and terminates prior to the QCD-confinement PT. The non-zero VEV $\langle \varphi \rangle \neq 0$ reproduces the SM Higgs mass term in Eq. (86). Thus, the electroweak (EW) PT is of second order and takes place in the common way. Depending on whether $T_\star > T_{\mathrm{EW}}$ or $T_{\mathrm{EW}} > T_\star > T_{\mathrm{QCD}}$, the EWPT will happen either 'on time' or delayed, respectively.

Combined first-order EW-QCD PT. If $T_\star < T_{\mathrm{QCD}}$, the quarks will condensate at T_{QCD}, i.e. the condensate's expectation value will then be $\langle q\bar{q} \rangle \neq 0$. As a result, the *zero temperature* effective potential V_{eff} in the h-direction gains a new term of the form $\propto - \sum_{\mathrm{q}} y_{\mathrm{q}} \langle q\bar{q} \rangle h / \sqrt{2}$, where y_{q} are the quarks' Yukawa couplings and h is the SM Higgs field [1, 2]. This additional term destabilizes the effective potential in terms of a small non-zero global minimum, which can be estimated by $v_{\mathrm{QCD}} = \langle h \rangle_{\mathrm{QCD}} = (y_{\mathrm{t}} \langle t\bar{t} \rangle / \sqrt{2} \lambda_{\mathrm{H}})^{1/3} \sim \mathcal{O}(100$ MeV$)$. Thus, if the QCD confinement PT is assumed to be of first-order, the result would be a first-order EWPT triggered by a fist-order QCD confinement PT. Regarding the symmetry breaking in the φ-direction (B − L-PT), we have to consider the effective potential below the QCD temperature T_{QCD}, which is given

by [2]

$$V_{\text{eff}}(T < T_{\text{QCD}}) \;=\; V_{\text{eff}}(T > T_{\text{QCD}}) - \frac{\lambda_{\text{H}\phi}}{4} v_{\text{QCD}}^2 \varphi^2 \,, \tag{95}$$

where $V_{\text{eff}}(T > T_{\text{QCD}})$ is the effective potential for temperatures above the QCD temperature from Eq. (87). The new term in Eq. (95) has a negative sign, meaning that it competes with the *thermal* 1-loop correction that produces the thermal potential barrier. We then have two situations: In the case where the negative term dominates, the thermal potential barrier will 'melt' such that the $B - L$-PT will be of second order. In the opposite case, its nature will be of first-order (for comparison, see Fig. 5 and Section 2.3.3).

Although this is a very fascinating topic, the treatment of the combined EW-QCD PT is not in the scope of this work. We will focus on performing calculations of the GW spectra for the the first-order $B - L$-PT case.

4 Numerical implementation

In this work, we use the programming language *Python* with its widely used libraries: `numpy`, `scipy`, `statistics` and `matplotlib`. Integrations were performed by using the `scipy ode` solver ($\texttt{rtol} = 10^{-5}$) or, in case of discrete integrals, via Riemannian summation method. Root finding tasks were mostly done with a self-coded bisection method, but sometimes also with the `fsolve` or `minimize` function from `scipy.optimize`.

4.1 How to find the *bounce* or *critical bubble* (or not)

To calculate the critical bubble (profile) or bounce, one has to solve the so-called bounce equation with the acoording boundary conditions (see Section 2.3.3).

$$\text{Bounce equation:} \qquad \frac{d^2\varphi}{dr^2} + \frac{2}{r}\frac{d\varphi}{dr} = \frac{dV_\text{eff}(\varphi, T)}{d\varphi}, \tag{96a}$$

$$\text{Boundary conditions:} \qquad \frac{d\varphi}{dr}\Big|_{r=0} = 0, \quad \lim_{r\to\pm\infty}\varphi(r) = 0. \tag{96b}$$

This differential equation is analogous to the equation of motion of a classical *'particle'* φ moving in the negative potential $-V_\text{eff}$[32]. Pictorially, one can think of the particle starting at some point close to the true vacuum rolling down the potential until it reaches the false vacuum in an infinite time. With this picture, the problem transforms to an initial value problem where one has to find the initial condition φ_init such that the particle φ lands exactly in the minimum at the end. The typical approach to this kind of problem is called *overshoot-undershoot-method*: An initial value guess is made in each iteration and a root finding algorithm is applied to successively get closer to the correct initial value (guess). Here, overshooting corresponds to the case where our initial value guess was too high such that the particle arrives in the negative minimum. Undershooting happens when our guess was too low and the particle lands in the positive minimum. Speaking of code, this procedure can be divided into two algorithms working together: the *solver* method which solves the differential equation, and the *finder* method that tries to find the correct initial value. Eventhough this technique sounds straightfoward, the unstable nature of this solution makes it impossible to find the exact solution numerically - an epsilon lengthed deviation around the correct initial value will lead to an over- or undershooting. Hence, the result of our calculation will always be a solution that either over- or undershoots the exact one, which is showed in Fig. 13. How can we cope with this unpleasant insight and obtain a solution we can further work with? The answer is rather simple: Since we know how the solution should behave and look like, i.e. be strictly decreasing and positive for all r, we can implement an abort criterion for

---

[32]Our effective potential is mirror-symmetric w.r.t the V-axis. Note that the true vacuua are now the global maxima and the false vacuum is the local maximum of the potential $-V_\text{eff}$. The thermal barriers correspond to the local minima of $-V_\text{eff}$.

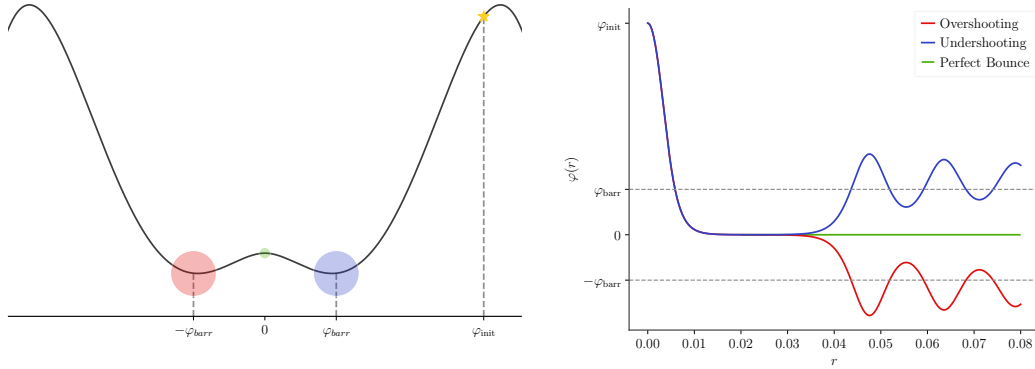[33]A nice explanation of this problem can also be found in [32].

Figure 13: Scheme of the over- and undershooting process.[33]

our integration solver such that it stops running if the solution starts to increase again or becomes negative at some point. Thus, for futher calculations, we will use the best possible solution which we simply cut off at this *abort point.*

As for the root finding method, the bisection algorithm is suitable since it is designed for problems with only one root in a specific known interval. This method divides the initial interval $[a, b]$ in two halfs and checks if the midpoint c is the root. If this is not the case, the midpoint will be set as the new boundary point of the new interval, $[a, c]$ or $[c, b]$. In our problem, we know the initial value must be $\varphi_{\text{init}} \in [\varphi_{\text{min}}(T), \varphi_{\text{max}}(T)]$ where $\varphi_{\text{min}}(T) \equiv \varphi_{\text{barr}}(T)$ and $\varphi_{\text{max}}(T) = 0.999\, \varphi_{\text{true}}(T)$. Furthermore, it is possible to explicitly compute the error of our solution via

$$r_{\text{bisec}}(n) \;=\; \left(\frac{1}{2}\right)^n |b - a| \;=\; \left(\frac{1}{2}\right)^n |\varphi_{\text{max}} - \varphi_{\text{min}}| \tag{97}$$

where n is the number of performed iterations. We can fix n such that the error r_{bisec} is relative, i.e. it scales appropriately with the value of the solution. Further calculations have shown that a choice of $n = 15$ is an appropriate choice.[34]

---

[34] As a final note, we want to mention that the nature of the bounce solutions at low temperatures (see Fig. 7) offers the opportunity to incorporate a temperature-dependent integration stepsize to minimize the needed working memory.

4.2 The percolation temperature $T_\star$

Now we turn to the calculation of the *percolation temperature* $T_\star$ where the average bubble is meant to collide. If one wanted to determine its value precisely, one would have to track the critical bubble's evolution with time until the collision takes place. Only then would it also be possible to explore the collision of bubbles of unequal size and unequal 'internal' field value $\varphi_{T>T_\mathrm{n}}(r=0)$. These kind of calculations would have to be performed on a spacetime lattice, which is a lot more complicated and time-consuming (see discussion in Section 2.3.4).

Hence, we want to follow a simplified approach: We neglect all those complications by averaging over all possible nucleation temperatures T_n and declare that the bubbles collide when the probability of finding a spot still being in the false vacuum drops to $P(T_\star) = \exp\left(-I(T_\star)\right)$ where $I(T_\star) = 0.34$ [2]. This temperature then marks the 'end' of the phase transition. To recall, the expression for the exponent $I(T)$ (see Section 2.3.3) reads

$$I(T) = \frac{4\pi}{3} \int_T^{T_C} \frac{dT'\ \Gamma(T')}{(T')^4\ H(T')} \left(\int_T^{\tilde{T}} \frac{d\tilde{T}}{H(\tilde{T})} \right)^3. \tag{98}$$

This integral has to be evaluated numerically in a discretized fashion. For that we perform a `while`-loop calculation by decreasing the lower bound of integration T stepwise until its value crosses the desired threshold, *or* the temperature reaches the temperature $T_\mathrm{QCD} \sim 100\,\mathrm{MeV} = 0.1\,\mathrm{GeV}$ of the QCD-confinement PT. We then have discrete lists of temperatures $\{T\}$, of the Hubble parameter $\{H(\{T\})\}$ and decay rates $\{\Gamma(\{T\})\}$. We can rewrite this integral to make its discretization a little more clear:

$$
\begin{aligned}
I(T) &= \frac{4\pi}{3} \int_T^{T_C} dT'\ \underbrace{\frac{\Gamma(T')}{(T')^4\ H(T')}}_{\equiv h(T')} \Bigg(\int_T^{\tilde{T}} d\tilde{T}\ \underbrace{\frac{1}{H(\tilde{T})}}_{\equiv g(\tilde{T})} \Bigg)^3 \\
&= \frac{4\pi}{3} \int_T^{T_C} dT'\ \underbrace{h(T') \left(\int_T^{\tilde{T}} d\tilde{T}\ g(\tilde{T}) \right)^3}_{\equiv f(T')} \\
&= \frac{4\pi}{3} \int_T^{T_C} dT'\ f(T')
\end{aligned}
\tag{99}
$$

One discrete value of the list $f_i = f(T_i) \in \{f(\{T\})\}$ reads

$$f_i = f(T_i) = h(T_i) \cdot \left[\sum_{j=1}^i (T_j - T_{j-1}) \cdot \frac{1}{2} \left(g(T_j) + g(T_{j-1}) \right) \right]^3. \tag{100}$$

After re-substituting $h(T) = \Gamma(T)/(T)^4 H(T)$ and $g(T) = 1/H(T)$, we can write down the total discretized expression for $I(T)$:

$$
\begin{aligned}
I(T) \;=\; & \sum_{i=1}^{N} (T_i - T_{i-1}) \cdot \frac{1}{2} \left[f_i + f_{i-1} \right] && (101) \\[2ex]
=\; & \sum_{i=1}^{N} (T_i - T_{i-1}) \cdot \frac{1}{2} \left\{ \frac{\Gamma(T_i)}{T_i^4 H(T_i)} \left[\sum_{j=1}^{i} (T_j - T_{j-1}) \cdot \frac{1}{2} \left(\frac{1}{H(T_j)} - \frac{1}{H(T_{j-1})} \right) \right]^3 \right. \\[2ex]
& + \left. \frac{\Gamma(T_{i-1})}{T_{i-1}^4 H(T_{i-1})} \left[\sum_{j=1}^{i-1} (T_j - T_{j-1}) \cdot \frac{1}{2} \left(\frac{1}{H(T_j)} - \frac{1}{H(T_{j-1})} \right) \right]^3 \right\}.
\end{aligned}
$$

Due to our finite T-stepsize, it is very unlikely to find the exact percolation temperature $T_\star$ which fulfils $I(T_\star) \equiv 0.34$. We will rather find some slightly smaller value $T_\star^{\mathrm{num}} \lesssim T_\star$ where $I(T = T_\star^{\mathrm{num}}) \gtrsim 0.34$.[35] Therefore, all calculations involving the computed value $T_\star^{\mathrm{num}}$, such as all the quantities needed for evaluating the GW spectrum in Section 2.3.4, will have an error due to $T_\star$'s calculation.

As a note for future code development, we would like to mention the importance of errors due to the lack of floating point precision. We noticed that the calculation of the three-dimensional Euclidean action S_3 (see Eq. (45)) is difficult in the low temperature regime, where the potential barrier cannot be properly resolved anymore. One has to extend the floating point precision to capture the existence of the barrier and to obtain correct results. We solved this problem by using the Python module `Decimal` with which we are able to arbitrarily extend the digits of floats.

---

[35]Here, the index *num* stands for *numerical (value)*.

5 Results

In this section, we want to give an account of the calculated percolation temperatures $T_\star$ of the models lying in our chosen parameter space. Moreover, we calculate the resulting GW spectra by using Eq. (72) and analyze their dependency on the gauge coupling g, the gauge boson mass $m_{Z'}$ and the reheating temperature T_{RH}. We also want to draw conclusions about their detectability with regards to the upcoming LISA experiment by computing the signal-to-noise ratios and comparing our results to its *power law integrated curve* (PLI). The latter will always be displayed as a grey curve in the GW energy density plots. Note that the GW spectra which overlap with the PLI are in principle detectable since they have a SNR of $\rho > \rho_{thr}$.

All heatmaps have been generated by using the `tikz` package from LATEX and its *bilinear* interpolation function.
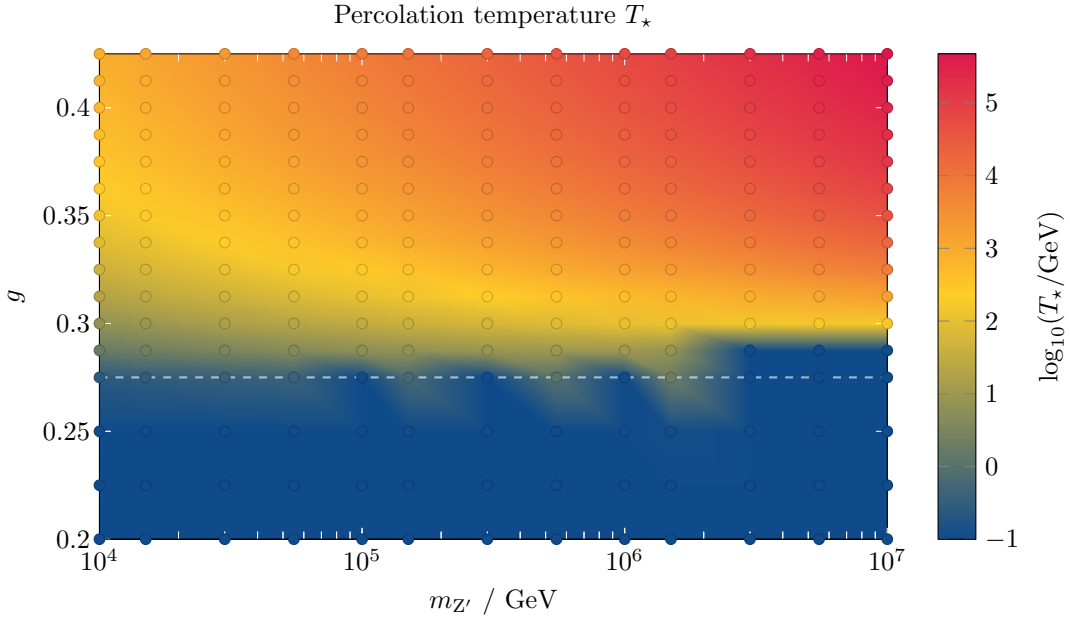
5.1 Percolation temperatures $T_\star$

Figure 14: $T_\star$ for parameter space $g \in [0.2, 0.425]$ and $m_{Z'} \in [10^4, 10^7]$. The values which were not explicitly calculated were interpolated by using **bilinear** interpolation. A white dashed horizontal line marks the point $g = 0.275$. The points in the plot correspond to the calculated points.

From Fig. 14, we see that the percolation temperature for our parameter space lies in the range of $T_\star \in [10^{-1} \text{ GeV}, 10^6 \text{ GeV}]$. Since we do not investigate the PT dynamics

for percolation temperatures $T_\star < T_{\text{QCD}}$ (see discussion in Section (3.2)), we have cut off to the $T_\star$-scala at $T_{\text{QCD}} = 10^{-1}$ GeV $= 100$ MeV.[36] With this being said, we clearly see that the first-order B − L-PT in the regime where $\alpha > 1$ happens prior to the QCD-confinement PT for $0.275 \lesssim g \lesssim 0.4$[37] almost independently from $m_{\text{Z}'}$ (region above blue area). This differs slightly from the results showed in [2] where they obtained a lower boundary of $g \gtrsim 0.25$, which is 10% lower than our result.

Another strong feature of the result is that $T_\star$ increases as g and $m_{\text{Z}'}$ increase such that we reach a maximum of $T_\star \sim \mathcal{O}(10^6$ GeV$)$ for $g = \max(g) = 0.425$ and $m_{\text{Z}'} = \max(m_{\text{Z}'}) = 10^7$ GeV.

5.2 GW power spectral density $h^2\Omega_{\text{GW}}$

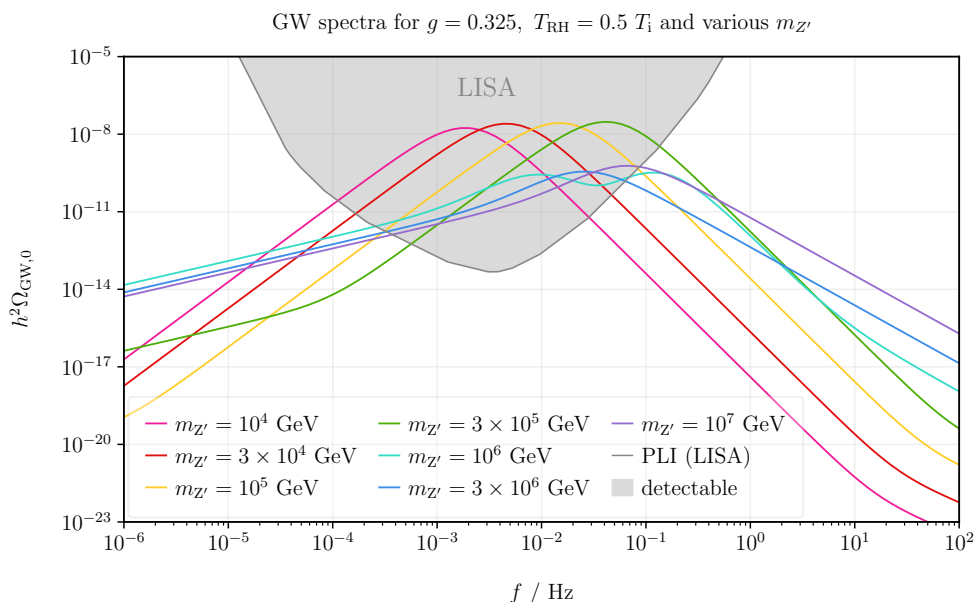Figure 15: GW spectra for a fixed gauge coupling $g = 0.325$ and various gauge boson masses $m_{\text{Z}'}$.

Varying the gauge boson mass $m_{\text{Z}'}$. We first compute the GW signal and vary the gauge boson mass $m_{\text{Z}'}$ while keeping the gauge coupling $g = 0.325$ and ratio of the reheating temperature and inflationary temperature fixed, i.e. $T_{\text{RH}} = 0.5\ T_{\text{i}}$. The result is shown in Fig. 15. Increasing the gauge boson mass $m_{\text{Z}'}$ leads to a shift of the

---

[36] Recall that a precise calculation of $T_\star$ below the QCD-temperature would require the incorporation of the additional term from Eq. (95) into the effective potential, which has not been done in this work. A computation without this term would lead to false results, which is why we prefer to cut it off at the QCD temperature.

[37] The upper boundary of $g = 0.4$ marks the limit until which $\alpha > 1$ and is taken from [2].

peak frequency to higher frequencies up until $f_{\text{peak}} \sim 10^{-1}$ Hz, which corresponds to the maximum of LISA's frequency domain. For $g = 0.325$ and $m_{Z'} \leq 3 \times 10^5$ GeV, we observe that the peak amplitude $h^2\Omega_{\text{GW}}^{\text{peak}}$ remains constant at the order of $\mathcal{O}(10^{-8})$. Greater gauge boson masses generate lower peak amplitudes which lie in the range of $h^2\Omega_{\text{GW}}^{\text{peak}} \in (10^{-11}, 10^{-8})$.

Note that at some points in the parameter space, we obtain multi-peaked GW spectra, such as the one for $g = 0.325$ and $m_{Z'} = 10^6$ GeV in Fig. 15 (turquoise), or for $g \in \{0.4, 0.425\}$ and $m_{Z'} = 10^5$ GeV in Fig. 16. The reason for this is that several GW contributions (see Section 2.3.4) might be equally strong such that their individual peaks become visible.
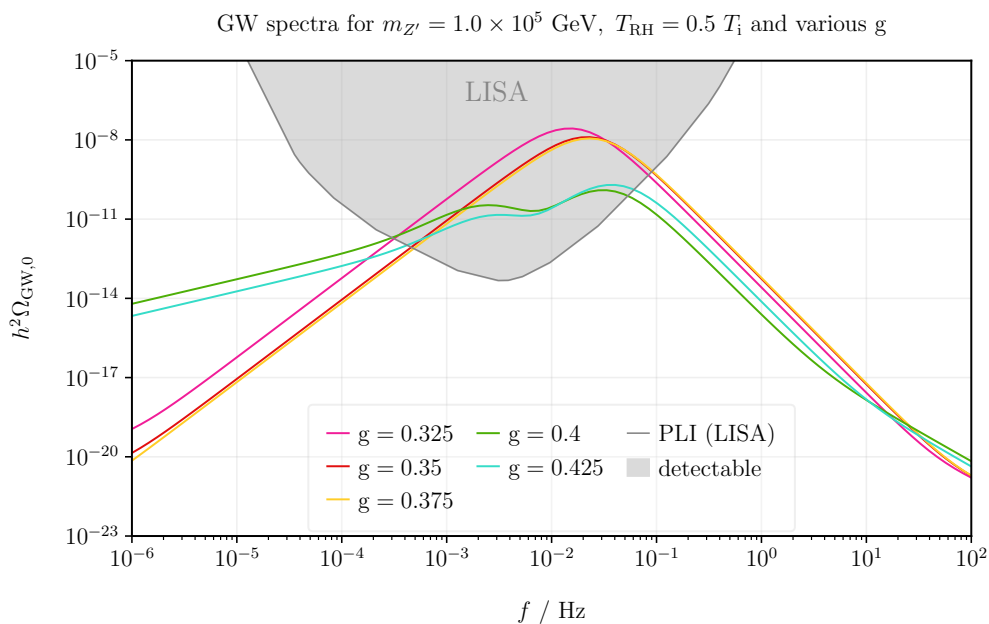

Figure 16: GW spectra for a fixed gauge boson mass $m_{Z'} = 10^5$ GeV and various gauge couplings g.

Varying the gauge coupling g. In Fig. 16 we plotted the GW energy density for a fixed gauge boson mass $m_{Z'} = 10^5$ GeV and $T_{\text{RH}} = 0.5\, T_i$ while varying the gauge coupling g. The first observation is that the peak frequency changes only slightly if we compare it to the observations from Fig. 15. It stays roughly the same at $f_{\text{peak}} \sim \mathcal{O}(10^{-2}$ Hz) (except the case where $g \in \{0.4, 0.425\}$). Secondly, we observe an increasing peak amplitude $h^2\Omega_{\text{GW}}^{\text{peak}}$ for increasing g.

Varying the reheating temperature T_{RH}. Here, more precisely, we vary the ratio between reheating temperature T_{RH} and the inflationary temperature T_{i}, i.e. $T_{\mathrm{RH}}/T_{\mathrm{i}}$, since it is a model-independent[38] quantity. This is shown in Fig. 17, where we chose a benchmark point of $g = 0.325$ and $m_{\mathrm{Z}'} = 10^4$ GeV. An increasing reheating temperature results in an increase of the peak amplitude $h^2\Omega_{\mathrm{GW}}^{\mathrm{peak}}$ as well as of the peak frequency f_{peak}. Recall from Section 3.2 that the inflationary temperature T_{i} is the upper bound for the reheating temperature T_{RH}. This means that the maximum possible amplitude for this benchmark point is $h^2\Omega_{\mathrm{GW}}^{\mathrm{peak}} \in (10^{-8}, 10^{-7})$.
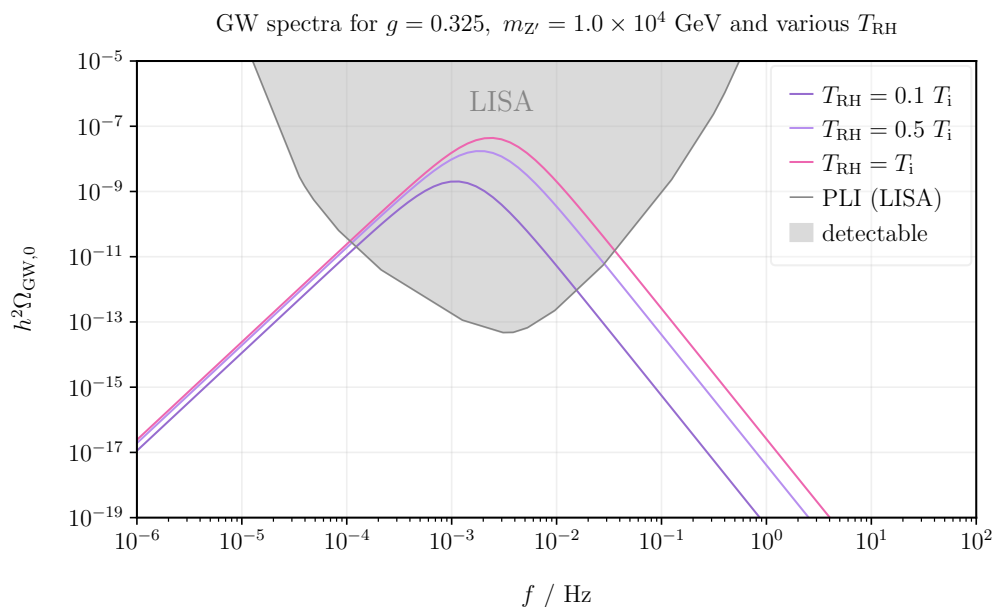

Figure 17: GW spectra for a fixed benchmark point $g = 0.325$, $m_{\mathrm{Z}'} = 10^4$ GeV and various reheating temperatures $T_{\mathrm{RH}} \in \{0.1\, T_{\mathrm{i}},\ 0.5\, T_{\mathrm{i}},\ T_{\mathrm{i}}\}$. The GW spectra's amplitude and peak frequency increase as T_{RH} increases.

▶ Let us summarize our first conclusions:

I The peak frequency f_{peak} of the GW spectra increases as we increase the gauge boson mass $m_{\mathrm{Z}'}$ or the reheating temperature T_{RH}. An increase in the gauge coupling g also slightly increases the peak frequency – however this effect is way smaller than the previously mentioned ones.

II The amplitude $h^2\Omega_{\mathrm{GW}}^{\mathrm{peak}}$ rises as we decrease the gauge coupling g as well as the gauge boson mass $m_{\mathrm{Z}'}$, or increase the reheating temperature T_{RH}.

III The largest amplitude is to be expected when $T_{\mathrm{RH}} = T_{\mathrm{i}}$. This corresponds to the

---

[38]With *model-independent* we mean that the quantity neither depends on g nor on $m_{\mathrm{Z}'}$.

case where (almost) all the scalar field energy is instantaneously transferred to the thermal radiation bath via friction on the bubble walls.

5.3 Signal-to-noise ratio (SNR) ρ

The SNR ρ mathematically corresponds to the integral of the squared overlap of the calculated GW spectrum $h^2\Omega_{\mathrm{GW}}$ w.r.t. the noise strain power spectral density $S_{\mathrm{LISA}}^{\mathrm{eff}}$ (see Eq. (79)). It will be maximal if the GW spectrum has a large amplitude and if its peak frequency lies approximately in the middle of the LISA frquency domain $f_{\mathrm{LISA}} = [10^{-5}\ \mathrm{Hz}, 1\ \mathrm{Hz}]$. By using our first conclusions drawn in Section 5.2, we can therefore expect the highest SNR values to appear in the parameter space region where the gauge coupling g and $m_{Z'}$ are rather small (bottom left corner in Fig. 14). Note that in the following plots, we will consequently leave out the parameter region below $g < 0.275$ in which $T_\star \leq T_{\mathrm{QCD}}$, since we do not calculate any GW spectra for this case.

In Fig. 18, we plotted the SNR ρ for our parameter space and $T_{\mathrm{RH}} = 0.5\ T_{\mathrm{i}}$. We find that it lies in the interval $\rho \in [28, 90739558]$, which is given by the minimum and maximum of the calculated SNR values, respectively. As a consequence, all of our calculated GW spectra must be detectable by the LISA experiment, since $\rho > \rho_{\mathrm{thr}} = 10\ \forall\ (g, m_{Z'}) \in [10^4\ \mathrm{GeV}, 10^7\ \mathrm{GeV}] \times [0.275, 0.425]$. This result strongly differs from [2], where they found that the region in the vicinity of maximal g and $m_{Z'}$ is not detectable by LISA. Note that our calculated SNR values are generally larger than compared to [2]. Despite these differences, the overall pattern is in accordance with the results from [2]:
The highest SNR values indeed seem to concentrate in the region where g and $m_{Z'}$ are small, which is a confirmation of our predictions. However, we also find very high values in the vicinity of $g = 0.275$ and $m_{Z'} \in [10^6\ \mathrm{GeV}, 10^7\ \mathrm{GeV}]$. The lowest SNR values are located in the area where g and $m_{Z'}$ are maximal. As we already know from the previous section, high gauge couplings g and gauge boson masses $m_{Z'}$ decrease the amplitude and increase the peak frequency, leading to an overall reduction of the overlap between the GW spectrum and $S_{\mathrm{LISA}}^{\mathrm{eff}}$ and thus a smaller SNR. Notice also the blurred areas in Fig. 18 in which it is being interpolated between the yellow and blue color, e.g. the regions $R_1 = [10^6\ \mathrm{GeV}, 10^7\ \mathrm{GeV}] \times [0.3, 0.35]$ and $R_2 = [10^5\ \mathrm{GeV}, 10^6\ \mathrm{GeV}] \times [0.35, 0.4]$. These correspond to the areas where we observed multi-peaked GW spectra in Fig. 15 and 16. In these cases, one of the corresponding peak frequencies can already lie (almost) outside LISA's frequency domain, whereas the other one is still able to create an overlap with $S_{\mathrm{LISA}}^{\mathrm{eff}}$. This way, the total overlap region might still be sizeable, resulting in a larger SNR value. Lastly, we want to discuss some potential error sources that can also lead to deviating results from [2]: The entire theory presented in Section 3 is based on the effective potential V_{eff} (see Eqs. (87) - (91)) from [30] whose shape is scaled by our model parameters g and $m_{Z'}$. The *zero-temperature* contrubution consists of the tree-level term and the Coleman-Weinberg potential (91). Although we qualitatively compare our results to the ones from [2], it is important to mention that the authors have used the *1-loop renormalisation-group (RG)-improved scalar potential* with

the RG-scale $\mu = m_t$ (top-quark mass) instead. Since the effective potential is connected to any other relevant quantity in our equations, an error propagation is inevitable. In addition to that, we have the usual erros due to finite numerical precision as well as the additional errors due to the finite T-stepsize in the $T_\star$ calculation (see Section 4), which is involved in the computation of $R_\star$ (see (50)) and thus in the evaluation of the GW spectra (see Eqs. (56) - (58)). Due to this concatenation of the used formulas, it is difficult to estimate an absolute error of our results.

However, as we have seen, the majority of our final results coincides with the results which were obtained independently in [2].
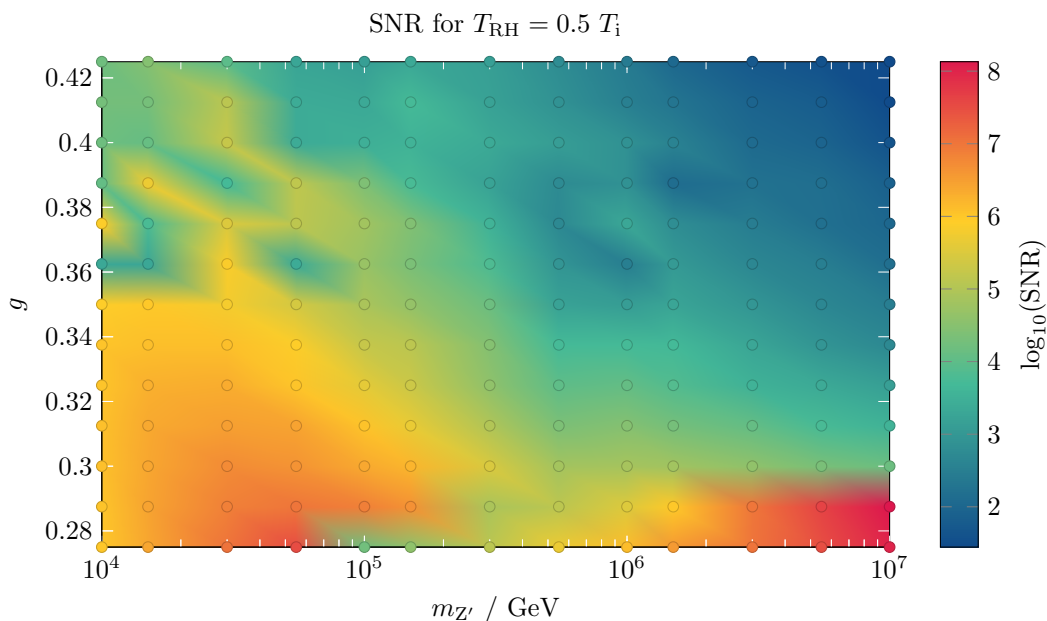

Figure 18: Heatmap of the SNR ρ for $T_{\mathrm{RH}} = 0.5\ T_{\mathrm{i}}$. Note that the small red area in the lower right corner which indicates extremely high SNR corresponds to the dark blue region in Fig. 14 where $T < T_{\mathrm{QCD}}$.

6 Conclusion

In this work, we have studied the $B - L$-SM extension within which we could find possible answers to some of the burning open questions in particle physics and cosmology. The conformal symmetry of the model provides an elegant mechanism to solve the Hierachy problem: the SM Higgs mass is dynamically generated by the $B - L$-symmetry breaking of the newly introduced scalar field φ. This eventually opens the door to multiple different cosmological scenarios (see Section 3.2) in which first- and second-order cosmological PTs are possible. The most interesting cases among them are a first-order $B - L$-PT that occurs before the QCD-confinement PT, and a first-order combined EW-QCD PT. We have learned that we can probe our theory by predicting and observing the GWs originating from the dynamics of these first-order PTs.

The goal of this work was to calculate the expected GW spectra and to evaluate the SNR to draw conclusions regarding their detectability with the future GW obervatory LISA.

Our final results indicate that a first-order $B - L$-PT in the regime[39] where $\alpha > 1$ takes place for gauge couplings $0.275 \lesssim g \lesssim 0.4$ and any gauge boson mass $m_{Z'} \in [10^4 \text{ GeV}, 10^7 \text{ GeV}]$. We find that its generated GWs should also be detectable by the future LISA experiment, since their SNR $\rho > \rho_{\text{thr}}$.

7 Outlook

The next extension of our code could be the implementation of the additional linear Higgs terms (see Eq. (95)) in the effective potential in order to study the dynamics and GW production of the combined EW-QCD PT. Moreover, our current research explores the possibility of baryo- or leptogenesis mechanisms within the $B - L$-SM extension to try explaining the mystery of today's matter-antimatter asymmetry. The question whether the new right-handed neutrinos in this theory can be suitable candidates for dark matter is also still not answered. Lastly, it would be interesting to learn more about the circumstances that lead to multi-peaked GW spectra in ceratin regimes (see Fig. 15 and 16).

---

[39] Note that this corresponds to the parameter space $(g, m_{Z'})$ we considered in Sec. 5.

A   Parameter dependence of the effective potential

Here, we shortly want to demonstrate how the variation of the gauge coupling g and gauge boson mass $m_{Z'}$ changes the shape of the effective potential $V_{\text{eff}}(\varphi, T)$ from Eq. (87)(see Fig. **??** and 20).
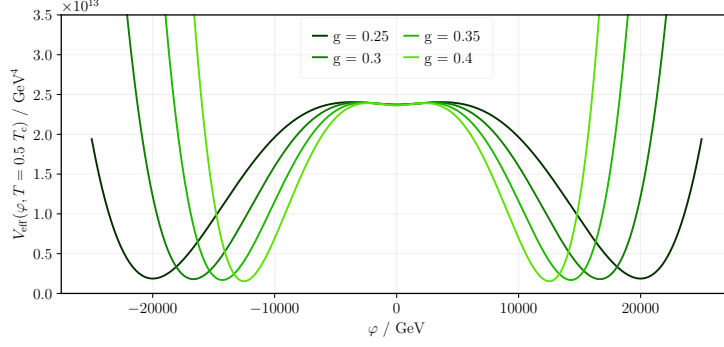

Figure 19: Effective potential $V_{\text{eff}}(\varphi, T = 0.5T_{\text{c}})$ for $m_{Z'} = 10^4$ GeV and various couplings g. As we can see, an increasing gauge coupling only squishes the potential such that the non-zero VEV decreases. The order of magnitude of the effective potential stays unaffected.
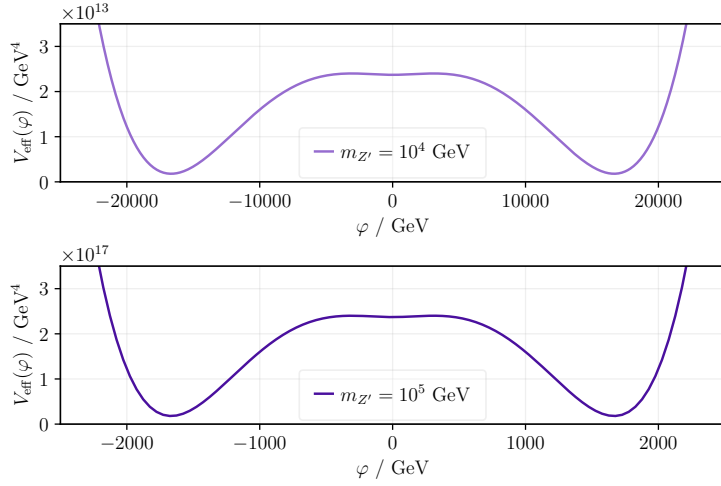

Figure 20: Effective potential $V_{\text{eff}}(\varphi, T = 0.5T_{\text{c}})$ for $m_{Z'} = 10^4$ GeV and various couplings g. In the lower plot, we observe that an increase in the gauge boson mass $m_{Z'}$ also squishes the effective potential which leads to smaller non-zero VEVs. Additionally, it increases the order of magnitude of the effective potential.

Aknowledgements

My plan was never actually to study physics, but somehow, three and a half years later, *this* happened! I am very grateful to have learned at least a little of how our fascinating world works – because it is so beautiful!

First of all, I want to thank Prof. Dr. Laura Sagunski for letting me work on this research topic that has plenty of potential for further explorations. It has been an interesting challenge to work in a research field that requires the understanding and connection of many different theories. Inside the working group, I was blessed to experience an open, welcoming and supportive environment. I am also thankful for having had the opportunity to get to know many scientists that are involved in the B07-project of the CRC-TR 211.

I thank Daniel Schmitt for his amazing co-supervision and support which included many helpful discussions, insights, and advises in coding.

I thank my parents, Barbara and Luis, for their eternal support and for making it possible for me to study what I am passionate about. I thank my sister Sara (aka little peanut) and my brother Nicolas for their love and support. I thank my friends for making these studies not as hard as they would have been without our friendships, which included loads of laughter - cheers to Charlotte, Dennis, Franz, Fritz, Greta, Janina, Josef, Maja, Marie, Lilith and Luise!
Special thanks go to my friend Janina who did an amazing job in proof-reading this thesis.

Last but not least, I thank Niklas Zorbach for his proof-reading, for being my everyday inspiration and for his emotional support from day one. It was you who got me into physics in the first place, and I will be always thankful for that. I love you!

References

[1] Satoshi Iso, Pasquale D. Serpico, and Kengo Shimada. QCD-Electroweak First-Order Phase Transition in a Supercooled Universe. *Phys. Rev. Lett.*, 119(14):141301, 2017.

[2] John Ellis, Marek Lewicki, and Ville Vaskonen. Updated predictions for gravitational waves produced in a strongly supercooled phase transition. *JCAP*, 11:020, 2020.

[3] Ryusuke Jinno and Masahiro Takimoto. Probing a classically conformal B-L model with gravitational waves. *Phys. Rev. D*, 95(1):015020, 2017.

[4] Schutz, Bernard F and Ricci, Franco. Gravitational Waves, Sources, and Detectors. 2010.

[5] Daniel Baumann. Lecture on general relativity. `http://cosmology.amsterdam/wp-content/uploads/2021/10/LectureScripts.pdf`, 2021.

[6] Leonardo Gualtieri. Gravitational waves from compact objects - lectures for the 2022 ggi apcg school. `https://agenda.infn.it/event/28760/contributions/164370/attachments/89036/119484/notes_gualtieri_1.pdf`, 2022.

[7] Michele Maggiore. *Gravitational Waves: 1. Theory and Experiments*. Oxford University Press, 2008.

[8] Moritz Breitbach, Joachim Kopp, Eric Madge, Toby Opferkuch, and Pedro Schwaller. Dark, Cold, and Noisy: Constraining Secluded Hidden Sectors with Gravitational Waves. *JCAP*, 07:007, 2019.

[9] Steven Weinberg. *Gravitation and Cosmology: Principles And Applications Of The General Theory Of Relativity*. Wiley, New York, 1972.

[10] C. L. Bennett, D. Larson, J. L. Weiland, N. Jarosik, G. Hinshaw, N. Odegard, K. M. Smith, R. S. Hill, B. Gold, M. Halpern, E. Komatsu, M. R. Nolta, L. Page, D. N. Spergel, E. Wollack, J. Dunkley, A. Kogut, M. Limon, S. S. Meyer, G. S. Tucker, and E. L. Wright. Nine-Year Wilkinson Microwave Anisotropy Probe (WMAP) Observations: Final Maps and Results. *The Astrophysical Journal Supplement Series*, 208(2):20, sep 2013.

[11] Daniel Baumann. Lecture on cosmology. `http://cosmology.amsterdam/education/cosmology/`, 2020.

[12] Bradely W. Carroll and Dale A. Ostlie. *An Introduction to Modern Astrophysics*. Pearson/Addison-Wesley, 2007.

[13] Nigel Goldenfeld. *Lectures on phase transitions and the renormalization group*. CRC Press, Taylor and Francis, 1992.

[14] Wolfgang Nolting. *Grundkurs Theoretische Physik 6: Statistische Physik.* Springer Berlin Heidelberg, 7 edition, 2014.

[15] Mikko Laine and Aleksi Vuorinen. *Basics of Thermal Field Theory.* Springer, 2018.

[16] Eric Madge Pimentel. *Phenomenology of New Physics Models at Colliders and in Gravitational Waves.* PhD thesis, Mainz U., 2020.

[17] Mark Hindmarsh, Marvin Lüben, Johannes Lumma, and Martin Pauly. Phase transitions in the early universe. *SciPost Physics Lecture Notes*, Feb 2021.

[18] Sidney Coleman and Erick Weinberg. Radiative corrections as the origin of spontaneous symmetry breaking. *Phys. Rev. D*, 7:1888–1910, Mar 1973.

[19] Sidney R. Coleman. The Fate of the False Vacuum. 1. Semiclassical Theory. *Phys. Rev. D*, 15:2929–2936, 1977. [Erratum: Phys.Rev.D 16, 1248 (1977)].

[20] Curtis G. Callan, Jr. and Sidney R. Coleman. The Fate of the False Vacuum. 2. First Quantum Corrections. *Phys. Rev. D*, 16:1762–1768, 1977.

[21] Andrei D. Linde. Decay of the False Vacuum at Finite Temperature. *Nucl. Phys. B*, 216:421, 1983. [Erratum: Nucl.Phys.B 223, 544 (1983)].

[22] Andrei D. Linde. Fate of the False Vacuum at Finite Temperature: Theory and Applications. *Phys. Lett. B*, 100:37–40, 1981.

[23] Arthur Kosowsky, Michael S. Turner, and Richard Watkins. Gravitational radiation from colliding vacuum bubbles. *Phys. Rev. D*, 45:4514–4535, Jun 1992.

[24] Arthur Kosowsky and Michael S. Turner. Gravitational radiation from colliding vacuum bubbles: envelope approximation to many bubble collisions. *Phys. Rev. D*, 47:4372–4391, 1993.

[25] Vedran Brdar, Alexander J. Helmboldt, and Manfred Lindner. Strong supercooling as a consequence of renormalization group consistency. *Journal of High Energy Physics*, 2019(12), dec 2019.

[26] Kiyoharu Kawana. Cosmology of Supercooled Universe. 1 2022.

[27] Official NASA Website of the Laser Interferometer Space Antenna (LISA).

[28] Pau Amaro-Seoane et al. Laser Interferometer Space Antenna. 2 2017.

[29] Michael E. Peskin and Daniel V. Schroeder. *An Introduction to Quantum Field Theory.* CRC Press Taylor and Francis Ltd., 2016.

[30] Cheng-Wei Chiang and Eibun Senaha. On gauge dependence of gravitational waves from a first-order phase transition in classical scale-invariant $U(1)'$ models. *Phys. Lett. B*, 774:489–493, 2017.

[31] Moritz Breitbach. Gravitational waves from cosmological phase transitions, 2022.

[32] Apreda, Riccardo and Maggiore, Michele and Nicolis, Alberto and Riotto, Antonio. Gravitational waves from electroweak phase transitions. *Nuclear Physics B*, 631(1-2):342–368, jun 2002.